May 2019

Tuning Size and Light Emission Characteristics of CDSES/ZNS Alloyed Core-shell Quantum Dots By Alcohol

John Casey Marnocha
University of Wisconsin-Milwaukee

TUNING SIZE AND LIGHT EMISSION CHARACTERISTICS OF $CdSe_{1-x}S_x$/ZnS ALLOYED CORE-SHELL QUANTUM DOTS BY ALCOHOL

by

J. Casey Marnocha

A Thesis Submitted in

Partial Fulfillment of the

Requirements for the Degree of

Master of Science

in Engineering

at

The University of Wisconsin-Milwaukee

May 2019

ABSTRACT

TUNING SIZE AND LIGHT EMISSION CHARACTERISTICS OF
$CdSe_{1-x}S_x$/ZnS ALLOYED CORE-SHELL QUANTUM DOTS BY ALCOHOL

by

J. Casey Marnocha

The University of Wisconsin-Milwaukee, 2019

Under the Supervision of Professor Nikolai Kouklin

In this thesis, a one-step isotropic down-tuning of the size of alloyed $CdSe_{1-x}S_x$/ZnS core-shell quantum dots is developed by vapor and liquid-phase etching using a $\sim 10:1$ isopropyl alcohol to water solution. The results of spectroscopic studies confirm continuous variation of the excitonic emission color from red to green for samples treated for up to 15 mins using a vapor-based method. According to HRTEM characterizations, the shift is consistent with a diameter reduction of quantum dots that proceeds at the average rate of ~ 1.3 Å/min. The emission intensity while seen to undergo an initial drop due to the shell removal, was to found to remain largely unchanged with increased treatment durations. The study presents a technologically viable alternative to adjusting the size and, in turn, the optoelectronic characteristics of core-shell quantum dots and nanocrystals in II-VI semiconductor systems.

For Sonja and Cadence...

TABLE OF CONTENTS

LIST OF FIGURES

LIST OF TABLES

ACKNOWLEDGEMENTS

I'd like to thank my advisor, Prof. Nikolai Kouklin, for the opportunity to explore my interests through research. I've come recognize you as a great steward of my educational experience due to willingness to generate truly constructive feedback. To my lab-mates, Elaheh Kheirandish and Niloufar Yavarishad, thank you for your collaboration within research and thesis preparation. Elaheh, this thesis would not have been possible without your characterization efforts along with Dr. Marvin Schofield and Prof. Heather Owen in UWM's HERTEM and SEM laboratories.

Sonja, my beloved soulmate, thank you for being a continuous grounding-force in my life. For your continued patience during my studies, your willingness to support my professional development, and the seemingly endless supply of nourishing meals, I express my deepest gratitude for your unwavering support. To my family, thanks for the words of encouragement and affirmation throughout this process. Dad, thank you for administering your infamous red-pen to my drafts.

To Dr. Margaret Guthrie and Dr. Danielle Berg, thank you for revealing the many tools and resources that helped me with this research. Not only are you terrific friends, but truly great role-models. To all of my classmates, especially, David Frailey and Alex Holmes, you've helped me in spirit and mind in more ways than you can imagine. It's been a humbling experience to learn alongside such brilliant minds.

I'd like to thank my professors at UWM, particularly, George Hanson and Ben Church, for being impactful educators and mentors. To my students, your affirmation has helped me realize my passion as a teacher and fellow learner. I am humbled and thank you all so very much.

Lastly, thank you to the Royal Society, Nature Photonics, and American Chemistry Society for permission to reprint select figures from your journals.

Chapter 1

Overview

1.1 Introduction

Colloidal quantum dots (QDs) have become increasingly investigated for their unique size-dependent optoelectronic properties. Considered zero-dimensional physical systems, QDs are small semiconductor crystals, typically of spherical shape and diameters on the order of $10^2 - 10^3$ atoms. Owing to their small size, QDs offer an ultimate degree of charge carrier and exciton confinement highlighted by broad absorption and bright emission spectra.[1–4]

Figure 1-1: QDs of increasing size, from left to right, emitting cyan through red. QDs are dispersed in solution and illuminated by UV light source.[5]

It has been well-documented that QDs exhibit single-band emission, i.e. atomic-like light emission, in the IR-UV spectral range. QDs are being used within applications once dominated by alternatives due to superior spectral tunability and stability. One of the bright examples is the replacement of organic dyes for *in vivo* and *in vitro* bio-medical labeling techniques.[6–9] Additionally, QDs are penetrating mainstream photo-emission markets in solid-state lighting and displays.[10–14] With the added benefit of high extinction coefficients and quantum yields approaching near unity, QDs are finding use in photo-detection technologies, photovoltaics, and solar cells[15–21] as well as single-photon sources and detectors.[22–25]

Nourished by demand of efficient and stable devices, the global quantum dots market is forecasted to grow rapidly, exceeding 60% annually.[5] Flat-panel display markets, for example, are expected to reach $135bn by 2020. Lighting alone constituted ∼7% of the total U.S. electricity consumption per the Energy Information Administration's 2017 reports, and is widely estimated to be ∼20% worldwide. High reported quantum efficiency is paving the way to higher power efficiency in QD-based LEDs and display backlights, up to twice as energy efficient than traditional LED-LCDs.[26] According to the US Department of Energy (DOE), widespread use of solid-state lighting could save ∼490 TWh of electricity by 2035, ∼$50bn per year in current electricity prices.[27] This is fueling government funding of a multitude of research initiatives involving the use of QDs, averaging an attractive 12-fold return on investment since 2000.[28] The economic and environmental motivation for continued development in QD-based technologies is clear.

1.2 Synthesis Techniques

The earliest investigations involved QDs created using stained-glass synthesis pathway. Such produced QDs were simply small particles embedded within glass matrices.[29] Nowadays, the two most common pathways to synthesizing QDs are through epitaxial or colloidal methods. Each of these methods offer distinct advantages and disadvantages, as discussed in the next sections.

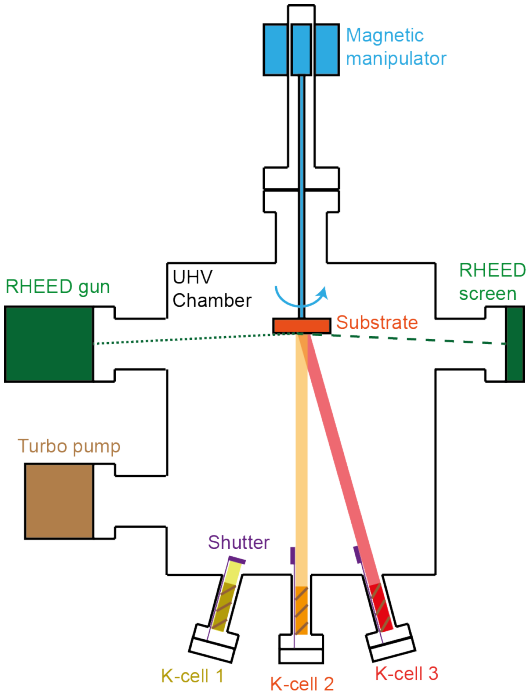

Figure 1-2: Schematic of molecular beam epitaxy chamber.

1.2.1 Molecular Beam Epitaxy

Molecular beam epitaxy (MBE) growth techniques are commonly used to fabricate quantum well, quantum dot, and heterojunction based devices from liquid or gaseous precursors.[30–32] A schematic of an MBE chamber is shown in Figure 1-2. The precursors containing elements of the target material are heated in separate Knudsen effusion cells (k-cells) and undertake a phase change, either from solid to liquid or liquid to vapor. The aperture is used to control the amount of precursor evaporating into the low pressure environment, forming individual atomic 'beams' generated from their respective k-cell. At ultra-low pressure, the mean free path is very large and the interaction with residual gas molecules remains limited. The sublimated atoms condense onto a substrate which is held at sufficiently high temperature to maintain mobility of the atoms and to allow the formation of the desired atom-thick film. In case of GaAs, the optimal substrate temperature is 500-600C.

To monitor the formation of the target structure during MBE, an electron beam is fired upon the substrate at an acute angle ($< 5°$) and the scattered electrons are detected. This *in situ* system is known as reflection high energy electron diffraction (RHEED) and is used

to monitor the state of growth during MBE. If the surface is non-uniform, the sensor picks up a smeared diffraction pattern. Once a crystalline monolayer has completed, the intensity of the diffraction pattern reaches a maximum. A single oscillation of RHEED intensity from local maximum to minimum to maximum is indicative that the formation of a monolayer has occurred. The process is repeated for each layer until the desired number of layers is formed, typically taking a minimum of 30 seconds to several minutes to complete each monolayer depending on the target semiconductor.

MBE substrate selection dictates the type of growth that occurs on its surface.[33] By employing a substrate with lattice constants identical to the semiconductor being grown, planar monolayers can be formed on the surface. To delineate patterns and to effect stronger quantum confinement of carriers, etching of the planar MBE-grown films is used. The etching process is used in conjunction with on optical (or electron) lithography to pattern a photoresist mask on the surface of the grown semiconductor film. Dry etching techniques have proven useful to form QDs on the order of 10-20 nm from planar films grown by MBE. Additionally, the connection to the substrate allows for direct charge injection, making synthesis of infrared lasers a prominent application. particularly useful for creating quantum well devices. The etching process, however, creates significant surface defects on the remaining QD structures, leading to degraded quantum yield and non-ideal emission bands.[34] Furthermore, variations in photoresist properties such as mask pattern, thickness, and sensitivity, all play into non-ideal emission behaviors. Thus, the large size and low quantum yield are both inhibitors to the adoption of such a method for many optoelectronic devices.

Alternatively, strain-induced methods use substrates with smaller lattice constants to create self-assembled, Stranski-Krastanov (SK), growth.[35,36] The strain in mismatched lattice constants localizes the desired semiconductor as small islets atop the substrate, removing the necessity of the post-growth etching as in the planar method. Mode-locked lasers and amplifiers have been made made using SK growth with telecommunication wavelengths near 1400 nm.[37] However, the islets tend to be irregularly spaced and typically have much

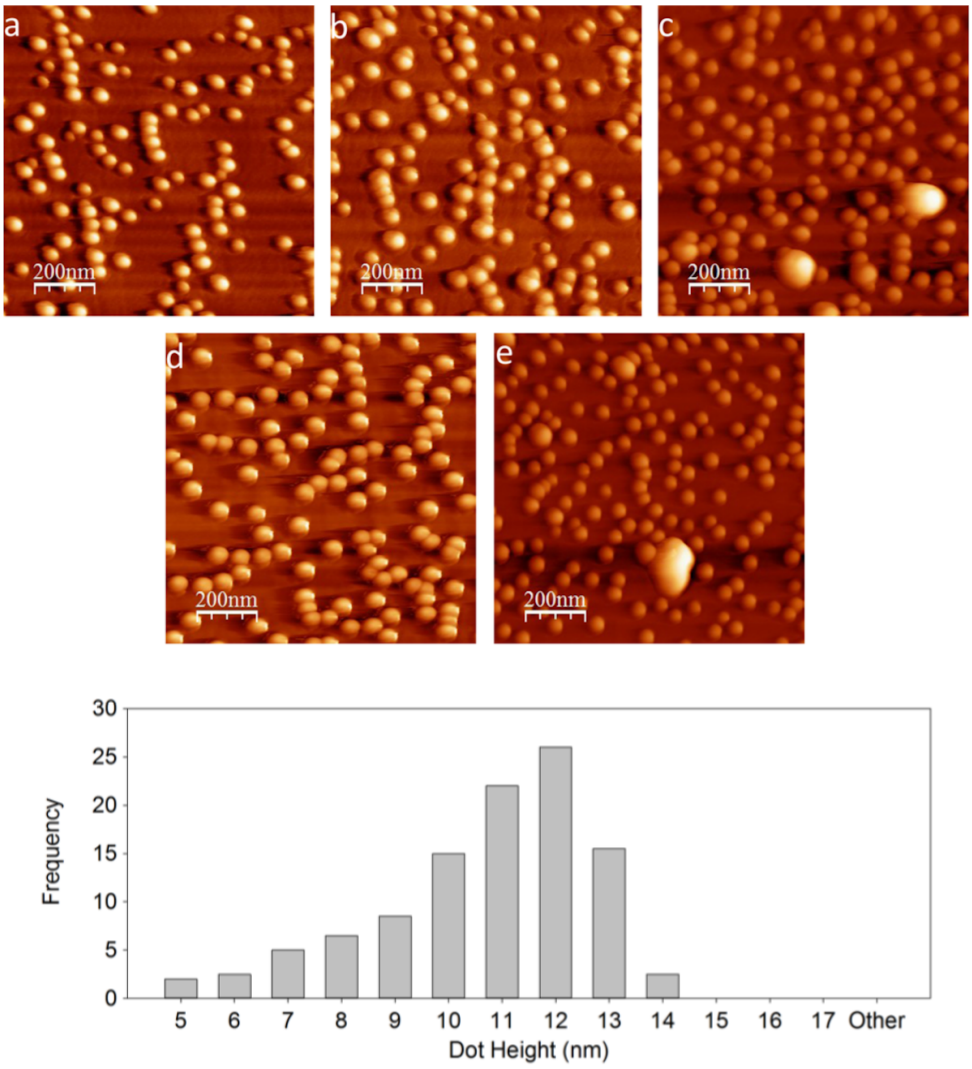

Figure 1-3: *Top:* Atomic force microscopy (AFM) images of InAs QDs grown by MBE using Stranski-Krastanov strained growth varying from 1.56 (a) to 2.53 (e) monolayers. *Bottom:* Example histogram showing statistical distribution of QD height (corresponding to top-left image). The islets do not require additional down-sizing after growth to exhibit confinement effects. However, the wide size and distributions can easily be seen.[32]

larger size and shape distributions, $\sim 10 - 30\%$, resulting in broad emission spectra. Figure 1-3 shows atomic force microscopy images of QDs grown in this manner.[38] The non-uniform spacing and variations in size are easy to see for each target size. When smaller islets are targeted, they can suffer from agglomeration due to Ostwald ripening, as in (c) and (e).

The use of IR-based fiber optics in communications continues to expand. Though relatively pure structures significant to IR lasing devices can be achieved using MBE growth methods, there are a number of significant drawbacks. Primarily, MBE only allows for growth on substrate surfaces, which must be very clean and crystalline to allow for the formation of high quality structures. Second, the impurity rate is highly sensitive to the vacuum environment. Any impurities in the chamber are likely to form defects in the resultant structures. The SK method creates strain defects throughout the crystal, and similarly, the planar post-growth etching process forms significant defects on the surface. These surface-bound structures, therefore, suffer from significantly reduced quantum yield compared to their colloidal counterparts. Furthermore, the size of the final structure is dictated by the mask resolution or the percentage of strain and temperature in SK growth. Therefore, continued research focusing on QD-based IR photoemitter and photodetectors make use of epitaxial grown QDs, such as In(Ga)As/GaAs. Ultimately, the low-throughput, relatively high cost, and surface bound QDs resulting from current MBE QD synthesis technologies act as barriers to their commercial viability.

1.2.2 Colloidal Growth

In the early 1980s, Brus began experimenting with reactions that produced colloidally grown semiconductor particles.[39,40] The experiments formed nanocrystals that demonstrated strong quantum confinement effects and motivated further research into creating and characterizing smaller and smaller semiconductor particles through the vehicle of colloidal synthesis. These early QDs suffered from wide size distributions, which in turn, obscured the true single-quantum dot emission characteristics. The true narrow-emission of quantum dots was confirmed through a number of experiments at low temperatures, fueling

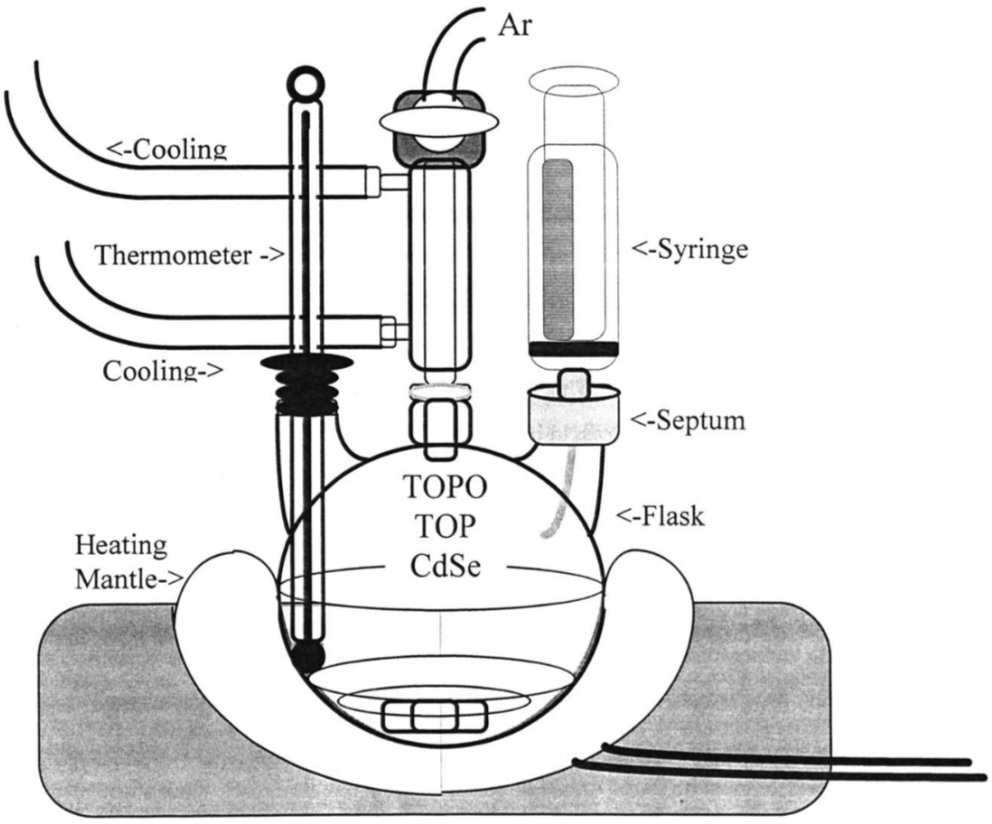

Figure 1-4: Schematic of apparatus used to grow CdSe through colloidal hot-injection method. Reagents (Cd and Se precursors) are mixed in the syringe then injected into the hot coordinating solvent resulting in many nucleation sites. The process is kept at high temperature, permitting the particles to grown in size with time. The process is quenched once the target size is reached.[44]

continued research initiatives.[41,42] The pioneering work completed by Murray *et al.* in 1993 established the colloidal growth technique widely utilized in modern QD synthesis.[43] This method relies on the hot-injection of organometallic reagents into a coordinating solvent contained in a reaction flask, the apparatus of which is depicted schematically in Figure 1-4.[44] Binary semiconductors, CdSe, CdS, and CdTe, were synthesized and exhibited high monodispersity under 10%, a previously unprecedented value.

To colloidally produce QDs, room temperature organometallic chalcogenides and cadmium reagents are injected into a hot-coordinating solvent ($\sim 320^{\circ}$C). The solvent is held at elevated temperatures, overcoming the nucleation threshold of the system. The reagents are injected rapidly into the vigorously stirred solvent, allowing temporally discrete nucleation sites to form. Through pyrolysis, the reagents decompose into their ionic elements and begin

to nucleate within the solvent. By decreasing the temperature in the flask shortly after the reaction starts, nucleation formation is suspended and the reaction enters a time-dependent growth phase, a beneficial consequence of adding room temperature reagents. The flask temperature is heated and maintained below the nucleation barrier ($\sim 280 - 300°\mathrm{C}$) during a growth phase. Although the nucleation sites are temporally discrete, the size distribution of the colloidally grown nanoparticles remains relatively narrow due to the thermodynamically driven Ostwald ripening process. The spontaneous process is caused by the relative instability of surface molecules to those in the interior. Since small particles have larger surface-to-volume ratios, they are 'digested' by larger particles, and if left to run indefinitely, the resulting particles would be quite large. The high temperatures also act to anneal the semiconductor during nucleation, resulting in highly crystalline, low-defect nanoparticles. The hot-injection method results in the rapid growth of a large number semiconductor particles exhibiting narrow size-distribution and, in turn, narrow emission spectra. By manipulating the temperature of the reaction solvent, as well as the allowed time of synthesis, particle size can be controlled. Aliquots of the systems can be taken and analyzed to characterize the state of QD formation. Once the target particle size is reached, the reaction vessel is quenched and the quantum dots can be precipitated from the coordinating solvent in powder form or re-dispersed in an appropriate solvent for later use.

Since this development, much research effort has gone into addressing monodispersity as well as surface chemistry.[45] Improvements include the addition of organic surfactants (ligands), originally trioctylphosphine oxide (TOPO) or trioctylphosphine (TOP), which act to moderately passivate the surface defects and evenly disperse the QDs.[46] Additionally, the application one or more passivating 'shells', consisting of wider band-gap material to better passivate non-radiative recombination sites has become common practice.[47,48] These topics are discussed in more detail in Chapter 2. Figure 1-5 depicts the optical range and narrow photoluminescence (PL) emission of common semiconductor QD species.[10]

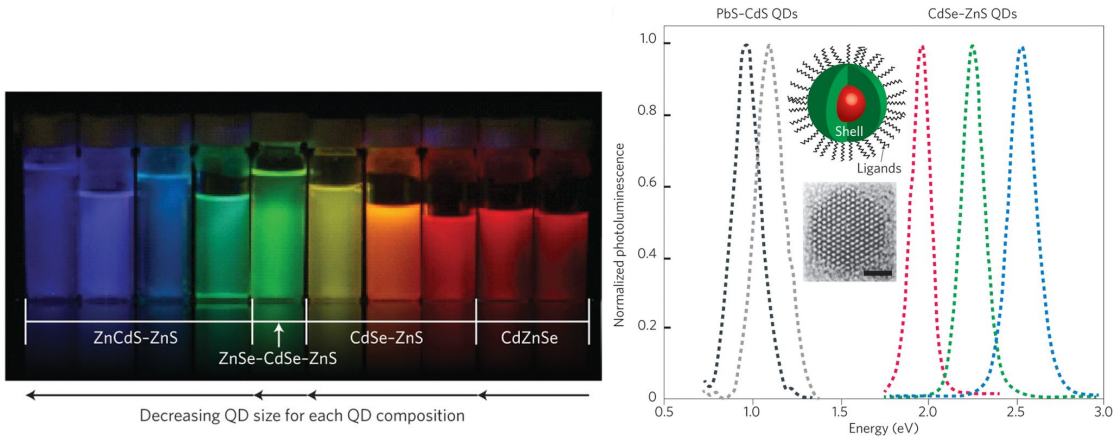

Figure 1-5: (Left) Solutions of colloidal QDs of varying size and composition exhibiting PL under optical (ultraviolet) excitation, demonstrating the size- and composition-dependent tunability of QD emission color. (Right) PL spectra of CdSe–ZnS and PbS–CdS core–shell colloidal QDs. The upper inset shows a schematic of a typical core–shell colloidal QD. The lower inset is a high-resolution transmission electron microscope image of a CdSe QD (scale bar, 1.5 nm). The figure shows the extension of this narrowband emission from blue to green to red and into the NIR. *Adapted with permission (2013) Nature Photonics.*[10]

Herein lies the favorability of colloidal QDs:

- simple synthesis method composed of precursors, surfactants, and solvents
- size tunable by controlling the durations of reactions at a given temperature
- compositional flexibility
- QDs are not bound to a surface and can be precipitated into powders
- QDs are conformable for post-growth processing
- most cost-effective method of QD synthesis

Additionally, two or more semiconductors can be alloyed to form materials with composition-dependent properties. The flexibility of precursor selection expands the applicability of the colloidal synthesis method to ternary or quaternary alloyed QDs.[49,50] Alterations to properties such as the bandgap, effective mass, and dielectric constant directly affect the allowed excitation energies, as derived in the next chapter. The relative alloy composition

alterations between two or more semiconductors offers an additional means of tuning the excitonic emission independent of QD size.

Binary colloidal synthesis (CdSe, CdS, etc...) primarily employs the aforementioned hot-injection synthesis technique. Alloyed QDs are primarily synthesized through a non-injection 'one-pot' approach. Where binary QD precursors are injected into a hot solvent, alloy QD precursors are mixed within the coordination solvent and brought up briefly to nucleation temperatures.[49] However, it is imperative to select alloy compositions that are similar in lattice constant and structural phase as well as precursors that are similar in reactivity. This reduces the formation of defects in the nanocrystal core, thus minimizing the prevalence of internal defect states that adversely affect free-exciton radiative recombination rates. The relative precursor mixture of chalcogenides (i.e. sulfur, selenium, and telluride) determines the final alloy content in the resulting QDs which exhibit near homogeneity throughout the core. For the examples of CdSeTe and CdSeS, alloy composition variation in conjunction with size-tuning has been shown to lie in the visible electromagnetic spectrum. Recently, CdSe and CdS precursors with similar reactivity have been used to form $CdSe_{1-x}S_x$alloyed cores that span the visible range.[51]

QD emission spectra can be tuned by a number of means. Parent material selection sets the lowest allowed energy of the QD while increasing confinement allows for a range of blue-shifting of the emission spectra. Parent material can be a single semiconducting material or alloyed for more complex stoichiometries. Additionally, colloidal QDs are synthesized in solution, making them stronger candidates for the many aforementioned applications versus their epitaxial counterparts. Commercial application trends are favoring colloidal QD synthesis due to favorable emission properties, owing to their optimized and stable luminescence. In general, synthesis of II-VI semiconductors is the least difficult compared to III-V and IV alternatives due to progressively more covalent bonding.

1.3 Motivation

Colloidal and Stranski-Krastanov (SK) epitaxial growth methods are bottom-up synthesis processes resulting in stand alone nanostructures with strong carrier confinement attributes. Though SK epitaxial methods are still used in specific cases such as building heterojunction lasers or single-photon detectors and sources, colloidal QDs dominate in biomedical, photovoltaic, and photoemission applications due to their solution-processability as well as relative ease and cost of manufacturing, amongst others.

Colloidally grown QDs are synthesized within solution in a time-dependent manner in which the final size is dependent on allowed growth time. Once the growth process is quenched, the growth subsides resulting in a QD of a particular size. However, the fine-tuning of the QD optoelectronic response must be set during this initial synthesis. It is apparent that growth of colloidal QDs with sizes below certain threshold is not possible due to Ostwald ripening.[52]

Until today, there have been no reports of a viable post-growth etching method for colloidal QDs that maintains shape, composition, and crystallinity of the QDs, ensuring no loss of PL induced by exciton non-radiative decay. It should be noted, although it has been shown that post-growth capping and shell modifications of colloidal QDs can alter their emission and absorption spectra, the main influence on confinement energies and optoelectronic response remains rooted in QD core size determined at the growth stage. Thus, the search for a complimentary procedure to controllably down-size high-quality colloidal QDs is warranted. The experimental methods developed and characterized herein aim to address this technological void.

1.4 Thesis Outline

The experimental work comprising this thesis makes use of colloidally grown $CdSe_{1-x}S_x/ZnS$ core-shell alloyed quantum dots. In Chapter 2, the optoelectronic properties of QDs are derived within the framework of effective mass approximation. Chapter 3 outlines the ex-

perimental processing methods employed to repeatably control optical blue-shifting in the QD emission. To quantify the effects of processing, Chapter 4 describes the characterization methods used to determine size, shape, crystallinity, and photoluminescence through HRTEM and PL. Lastly, the results of these characterization methods are discussed in Chapter 5. A short summary and potential applications of the thesis subject matter are presented in Chapter 6.

Chapter 2

Quantum Dots

QDs have shown significant promise for many optoelectronic and biomedical applications. The central attribute of semiconductor QDs is their size-tunable optoelectronic properties. Their small size promotes excitonic emission, i.e. high radiative recombination. This chapter reviews the solid-state and quantum mechanical constructs that describe such photophysical behavior.

2.1 Light Emission from Semiconductors

Generally speaking, semiconductors can luminesce through the absorption and subsequent emission of an incident photon.[53] When the photon is absorbed, an excited electron is promoted into the conduction band with the energy of the photon. When electron is promoted to the conduction band, a hole is formed in the valence band. At room temperature, the Coulomb attraction within the electron-hole pair is smaller than the thermal energy of the system, generally leading to formation of individual charge carriers. In this context, the excited electron experiences rapid relaxations, lowering its energy level through a series of non-radiative pathways between energy states within the conduction band – an example being through the dissipation of electron kinetic energy into the crystal lattice (phonons). Subsequently, the electron drops from the conduction band to the ground state (in the valence band) emitting a photon of equal energy to the energy of the gap (bandgap). The

recombination process is referred to as spontaneous emission, which varies from stimulated emission as in solid state lighting and lasers.

Considering a bulk semiconducting solid, there are two main categories of recombination pathways: intrinsic and extrinsic. Intrinsic recombinations are those that span the bandgap of the material and are a consequence of the ideal semiconductor structure and atomic composition, Figure 2-2 (a). Extrinsic recombination pathways are those due to defects, such as dopants or impurities in the material. The defect sites that occur in the otherwise forbidden bandgap region effectively lower the energy of emitted photons, Figure 2-2 (b) and (c).

For many optoelectronic device applications, use of semiconductor materials is preferred over incandescent sources, which operate at high temperature and radiate a wide range of wavelengths. Materials with an indirect bandgap require phonon assistance to emit a photon to ensure both momentum and energy conservations, Figure 2-1. Considering the photon as a mass-less particle, the required phonon is unlikely, lending to low radiative recombination probability.

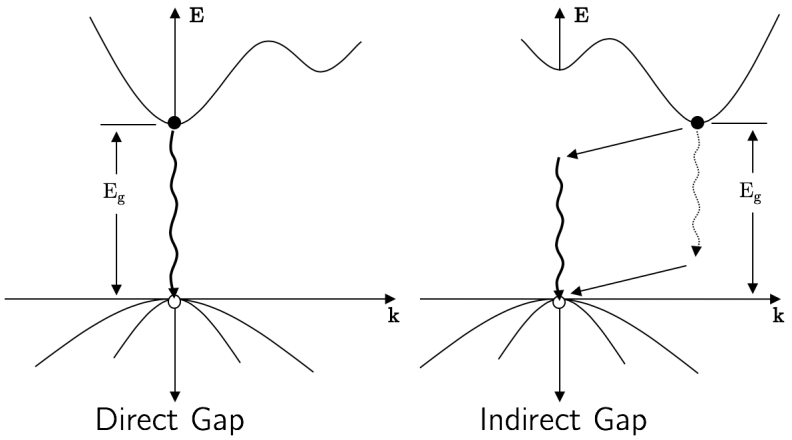

Figure 2-1: Example energy bands of direct (left) and indirect (right) semiconductors. The minimum energy difference between the upper conduction and lower valence band is the bandgap of the material, E_g. Indirect semiconductors require phonon assistance to spontaneously emit whereas direct semiconductors do not.

Conversely direct-gap semiconductors, do not need phonon assistance for radiative transitions. This leads to larger radiative recombination probability, or in other words, a much

higher quantum yield (QY)– the ratio of absorbed photons to emitted photons. Thus, in optoelectronic applications based on semiconductor QDs, we turn to direct gap semiconductors systems.

Though silicon has proven to be an important material for electronic devices, it is an indirect bandgap semiconductor making it a non-ideal choice for emissive systems.* In what follows, we primarily consider the direct gap II-VI semiconductors CdSe, CdS, and their alloy $CdSe_{1-x}S_x$, although a wide class of direct and indirect semiconductor materials have been prepared in nanocrystal form, including Si and Ge, III-V semiconductors (GaAs, GaP, InP), and I-VII semiconductors (CuCl, CuBr, AgBr).[3] CdSe and CdS have bulk room temperature bandgaps of 1.7 eV (red) and 2.42 eV (green), respectively, and their alloyed bandgap can be determined using the bowing formula,

$$E_{g(CdSeS)} = (1-x)E_{g(CdS)} - xE_{g(CdSe)} - bx(1-x), \quad b = 0.28 \text{ eV} \tag{2.1}$$

where x is the alloy content ratio and b is the bowing constant.[54] At normal temperature and pressure they crystallize in the hexagonal, wurtzite lattice (space group $P6_3mc$), but can also crystallize in the cubic, zinc-blende modification (space group $F\bar{4}3m$), although it is metastable under normal conditions.[55] For semiconductor QDs, these compounds dominate in systems that operate in the visible range.

Within the effective mass approximation (EMA), semiconducting materials with direct transition bandgap exhibit energy states in conduction and valence bands centered at $\mathbf{k} = 0$,

$$E_c(\mathbf{k}) = E_c(0) + \frac{\hbar^2\mathbf{k}^2}{2m_e^*} \quad \text{and} \quad E_v(\mathbf{k}) = E_v(0) - \frac{\hbar^2\mathbf{k}^2}{2m_h^*} \tag{2.2}$$

where $\mathbf{k}$ is the quasi-momentum of the charge carriers and m_e^* (m_h^*) is the effective electron (hole) mass. By modeling the energies as simple harmonic oscillators with masses affected by the periodic crystal structure, the density of allowed energy states form parabolic bands

*It should be noted that silicon QDs are being investigated, exploiting the loss of translational symmetry and momentum conservation in small systems as a means to generate excitons.

where their energy separation, $\hbar\omega$, for direct transitions is given by

$$\hbar\omega = E_c - E_v \tag{2.3}$$

$$= E_c(0) - E_v(0) + \frac{\hbar^2\mathbf{k}^2}{2m_e^*} + \frac{\hbar^2\mathbf{k}^2}{2m_h^*} \tag{2.4}$$

$$= E_g + \frac{\hbar^2\mathbf{k}^2}{2\mu^*} \tag{2.5}$$

where E_g is the bandgap and $\mu^{-1} = m_e^{*-1} + m_h^{*-1}$ is the reduced effective mass of the material. The separation of valence and conduction energy bands in a semiconductor dictates the minimum necessary energy for photon absorption to occur, taking the value E_g when $\mathbf{k} = 0$.

A third recombination pathway exists in which the electron-hole pair forms a quasiparticle called the exciton. The attraction of the exciton is the origin of the pronounced increase in probability of radiative recombinations compared to intrinsic and extrinsic pathways. Conditionally, for excitonic decay to occur, the exciton must remain intact within the semiconductor. This can be achieved by a system meeting one of the two following conditions: a) the thermal energy is to be less than the Coulombic exciton binding energy, or b) the system must prohibit dissolution of the exciton by some other means, i.e. by providing a confinement potential to spatial confine the electron-hole pair in the same region.

Excitonic emission has long been reported in bulk semiconductors when the thermal energy E_T is less than the binding energy.[56] For example, $E_T \sim k_B T$ at 110 K is 10 meV, which is less than the exciton binding energy for many semiconductors, such as CdSe and CdS with reported values of 15 meV and 28 meV, respectively.[57] However, this low temperature condition is unsuitable for most optoelectronic applications.

Therefore, semiconductor crystals must be small enough to spatially confine the exciton at room temperatures. The distance between the average location of the electron and hole is defined as the exciton Bohr radius, a_B and its value is derived in Section 2.3.1. Thus, the size of QDs must be at or less than a_B to keep the exciton stable. Of course, the size at which charges become confined varies from material to material and is dependent on

the quantum mechanics of the of charge carries and crystal structure. QDs comprised of cadmium chalcogenides, such as CdSe and CdS, have reported values of $a_B(CdSe) = 5.4$ nm and $a_B(CdS) = 2.7$ nm. This implies room temperature excitonic emission can be achieved at diameters near or below ∼10.8 nm and ∼5.4 nm for these materials, respectively.

Examples of radiative recombination pathways are depicted in Figure 2-2. Intrinsic recombinations from the conduction to valence band are shown in Figure 2-2 (a). Extrinsic recombinations from neutral acceptor and donor defect (or dopant) sites are shown in Figure 2-2 (b) and (c), respectively. Excitonic recombinations depicted in Figure 2-2 (d) and (e) are the idealized 'free' and captured 'bound' cases, respectively. Excitons can be bound, or captured, by neutral (D^0) or ionized (D^+) sites, for example. Finally, deep trap states, such as surface defects are shown in Figure 2-2 (f), the passivation of which are of much interest, and are discussed in the next section.

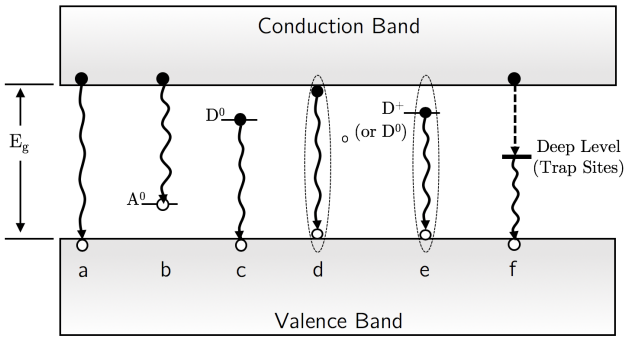

Figure 2-2: Radiative recombination pathway examples in semiconductors. (a) Intrinsic. (b) Extrinsic acceptor and (c) donor. (d) Excitonic free and (e) bound. (f) Deep trap site where the bottom transition is radiative, for example.

2.2 Quantum Yield and Efficiency

QDs offer exciton confinement, increasing the Coulombic potential between the electron-hole pair. This offers a gateway for excitonic emission at room temperature. For a confined system, such as the CdSe example depicted in Figure 2-3 (top), the electron and hole wave-functions primarily exist within the confines of a spherical potential well in the conduction and valence bands, respectively.[47] Since physical system potentials are finite, the wave-

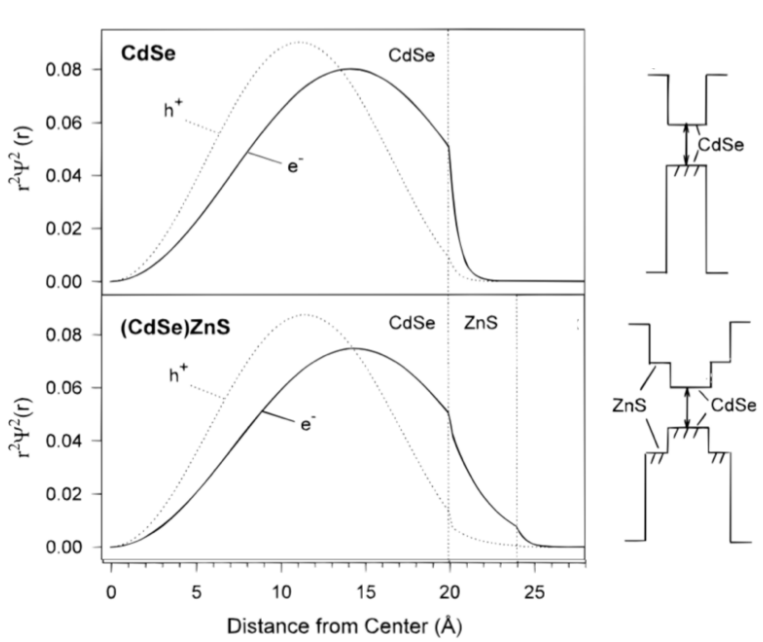

Figure 2-3: (Left) Electron and hole wavefunctions in a confined CdSe QD with (bottom) and without (top) a passivating ZnS shell. (Right) Corresponding energy diagrams with vertical axis as energy and horizontal axis representing spatial dimension of bare-core (top) and core-shell (bottom). *Adapted with permission, Copyright (1997) American Chemical Society.*[44]

functions technically leak into the surround space, but most importantly, the wavefunctions of the electron and hole overlap, increasing the probability of exciton decay. The offset of peak locations of these wavefunctions is the exciton Bohr radius and is dependent on the dielectric constant of the material. Upon further confinement, the wavefunctions are squeezed, forcing the wave functions to overlap further, increasing the excitonic radiative recombination probability.

The repeating semiconductor lattice within the QD core abruptly ends at the surface of the QD. The reconstruction of atomic bonds at the surface results in the formation of the surface-associated defect states within the band-gap of the semiconductor.[45,58] Bare-core QDs intrinsically have a high surface-defect to volume ratio $\eta \sim 1/a$ due to their small physical size. Initial attempts to 'passivate' involved the use of organic ligands, such as TOP and TOPO.

Alternatively, these surface defects can be 'passivated' by coating the core with a shell semiconducting material whose bandgap is larger than the core as to maintain confinement,

depicted in Figure 2-3 (bottom).[48,59] These are called 'core-shell' QDs. For the case of CdSe and CdS, ZnS shells have been routinely used to passivate the surface. The thickness of the shell plays an important role as the lattice mismatch of the core and shell invariably create strain defects that can act as exciton recombination centers. Furthermore, the leakage of the electron wavefunction is more pronounced in core-shell configurations. However, the significant decrease in otherwise abundant surface defect states promotes increased quantum yield from ∼10% for bare-core up to >95% for core-shell variants.[60]

Quantum yield (QY) is the ratio of absorbed photons to radiatively emitted photons by a system. QY is a central figure-of-merit for synthesized QDs and can be found by comparing emission to a known reference or through integrating sphere measurements. For example, taking the reference case, a dye with known QY is typically used. By matching the absorption characteristics of the dye sample with a QD sample, calibrated integrated photoluminescence emission (PL) measurements can be obtained. The following expression can then be used to solve for the QY of the QD,

$$\mathrm{QY_{QD}} = \mathrm{QY_{Dye}} \, \frac{I_{\mathrm{QD}}}{I_{\mathrm{Dye}}} \frac{n_{\mathrm{QD}}}{n_{\mathrm{Dye}}} \frac{F_{\mathrm{Dye}}}{F_{\mathrm{QD}}} \tag{2.6}$$

where I is the integrated PL emission, n is the refractive index of applicable solvents, and F is the fractional absorption (optical density) coefficient at the excitation wavelength, taking a value of 1-10.

In addition to tunability and QY, external quantum efficiency (EQE) is also key figure-of-merit attribute in photoemitting devices such as QD-based light emitting diodes (QD-LED)[4] and photovoltaic devices, such as solar cells.[19] EQE for an LED is defined as the ratio of LED emitted photons to the number of injected electrons, or in equation form,

$$\mathrm{EQE} = \frac{\text{emitted photons}}{\text{supplied electrons}} = \eta_r \; \chi \; \eta_{PL} \; \eta_{oc} = \mathrm{IQE} \; \eta_{oc} \tag{2.7}$$

where η_r is the ratio of injected electrons that form excitons, χ is the ratio of those excitons that have optical transitions,η_{PL} is the photoluminescence QY, η_{oc} is the ratio of photons

that are 'output coupled' from the device, and IQE is the 'internal quantum efficiency', which is independent of η_{oc}.[10] CdSe QDs exhibit a χ value near unity, which matches that of organic electroluminescent devices.[61] However, Auger recombinations, due to charging, as well as energy transfer amongst an ensemble of QDs can lead to self-quenching and can restrict the electroluminescent efficiency of QD-LEDs. With QY values reaching near unity, it is clear that IQE is technologically limited by η_{PL} and EQE is limited by η_{oc}, as well.

Conversely for a solar cell, EQE is the ratio of the number of generated electrons to the number of incident photons, or in monochromatic equation form,

$$\text{EQE} = \frac{\text{electrons harvested}}{\text{incident photons}} = \frac{E_p}{e^-}\frac{I}{P_{in}} \approx \frac{1240\ J_{sc}(\lambda)}{\lambda\ P_{in}} \tag{2.8}$$

where E_p is the energy of a single (monochromatic) photon at wavelength λ, e^- is electron charge, I is the generated current, P_{in} is the optical power of the source, and J_{sc} is the current density. The IQE is in respect to absorbed photons and is independent of the absorption of the system. Additionally, the power conversion efficiency (PCE) can be calculated using current-voltage measurements,

$$\text{PCE} = \frac{J_{sc}\ V_{oc}\ \text{FF}}{\int d\lambda\ P_{in}(\lambda)} \tag{2.9}$$

where J_{sc} is the short-circuit current density, V_{oc} is the open-circuit voltage, FF is the fill factor, and P_{in} is the incident optical power spectra as a function of wavelength λ. Increasingly being investigated are QD-based sensitized solar cells (QDSSC), which have recently recorded PCE values of $\sim 12-13\%$.[62] Limitations include electron injection and charge collection efficiencies. Interestingly, absorption of a photon at least twice the bandgap of the QD can produce multiple excitons, a process known as multiple exciton generation (MEG). This phenomena has been exploited using short wavelength excitation ($\sim$UV) to produce EQE values in excess of 100%,[63] an indication that PCEs exceeding the Shockley–Quessier efficiency limit (32.9% for single absorber) may be be possible in the future.

2.3 Derivation of Energy States

It is well understood that systems on the order of the de Broglie wavelength exhibit quantum mechanical, or wave-like, characteristics. The influence of crystal size and composition on emission properties of a material can be found by solving for the energy eigenstates of the system. The transition energy $\hbar\omega$ in the confined case is derived in the following sections. The effective separation of conduction and valence bands in a isotropically confined system is the sum of the intrinsic bandgap of the material E_g, the Coulombic exciton binding energy of the electron-hole pair E_B^n, and the confined energies of the electron and hole $E_{n,l}$,

$$\hbar\omega = E_g + E_B^n + E_{n,l} \tag{2.10}$$

of principle quantum number n and angular quantum number l. It is important to note, that the value of E_g in this case is the same intrinsic value as shown in Eq (2.5) for a direct material. However, the dispersion relation $E_g(\mathbf{k})$ is formally unsolvable due to lack of periodicity in the crystal.[64] This has the effect on the density of states $\rho(\mathbf{k})$ becoming independent of $\mathbf{k}$, as systematically depicted in Figure 2-4.

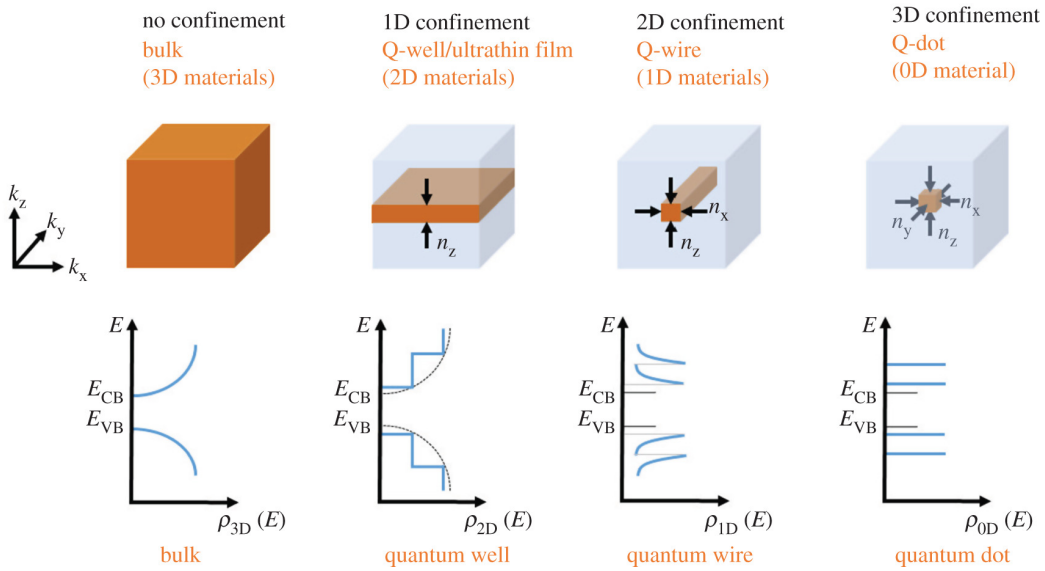

Figure 2-4: Schematic illustration of confinement and its effect on the idealized density of states. The energy levels of a 3D material are continuous whereas 0D material levels are discrete.[64]

2.3.1 Electron-Hole Interaction: Exciton Binding Energies

Given a sufficiently small system, there is a non-negligible interaction energy between the confined electron and hole pair (exciton) in the form of a Coulombic potential. To solve the steady-state Schrödinger equation for the allowed energies in a confined system such as the QD, the Hamiltonian takes on a hydrogen-like description,

$$\mathcal{H} = -\frac{\hbar^2}{2\mu}\nabla^2 + V(r_e, r_h) \tag{2.11}$$

where $\mu^{-1} = m_e^{*-1} + m_h^{*-1}$ is the reduced effective mass of the material, V is the potential, and r_e (r_h) is the average position of the electron (hole). The Coulombic potential between the electron and hole is,

$$V(r_e, r_h) = -\frac{e^2}{4\pi\epsilon|r_e - r_h|} = -\frac{e^2}{4\pi\epsilon a_{_B}} \tag{2.12}$$

where $\epsilon \equiv \epsilon_r\epsilon_0$ is the dielectric constant of the material and the exciton Bohr radius is $a_{_B} = r_e - r_h = r$. Exciton binding energy levels can again be solved for by way of the stationary Schrödinger equation. In the spherical coordinate system,

$$-\frac{\hbar^2}{2\mu}\left[\frac{1}{r^2}\frac{\partial}{\partial r}\left(r^2\frac{\partial\psi}{\partial r}\right) + \frac{1}{r^2\sin\theta}\frac{\partial}{\partial\theta}\left(\sin\theta\frac{\partial\psi}{\partial\theta}\right) + \frac{1}{r^2\sin^2\theta}\frac{\partial^2\psi}{\partial\phi^2}\right] - \frac{e^2}{4\pi\epsilon r}\psi = E\psi \tag{2.13}$$

$$\frac{1}{r^2}\frac{\partial}{\partial r}\left(r^2\frac{\partial\psi}{\partial r}\right) + \frac{1}{r^2\sin\theta}\frac{\partial}{\partial\theta}\left(\sin\theta\frac{\partial\psi}{\partial\theta}\right) + \frac{1}{r^2\sin^2\theta}\frac{\partial^2\psi}{\partial\phi^2} + \frac{2\mu}{\hbar^2}\left(E + \frac{e^2}{4\pi\epsilon r}\right)\psi = 0 \tag{2.14}$$

Turning to the separation of variables technique, we can assume a product solution of radial and angular functions such that,

$$\psi(r, \theta, \phi) = R(r)Y(\theta, \phi). \tag{2.15}$$

Separating out the radial and angular terms,

$$\frac{1}{R}\frac{\mathrm{d}}{\mathrm{d}r}\left(r^2\frac{\mathrm{d}R}{\mathrm{d}r}\right)+\frac{1}{Y\sin\theta}\frac{\partial}{\partial\theta}\left(\sin\theta\frac{\partial Y}{\partial\theta}\right)+\frac{1}{Y\sin^2\theta}\frac{\partial^2 Y}{\partial\phi^2}+\frac{2\mu r^2}{\hbar^2}\left(E+\frac{e^2}{4\pi\epsilon r}\right)=0. \quad (2.16)$$

Separating into radial and angular equations, respectively,

$$\frac{\mathrm{d}}{\mathrm{d}r}\left(r^2\frac{\mathrm{d}R}{\mathrm{d}r}\right)+\frac{2\mu r^2}{\hbar^2}\left(E+\frac{e^2}{4\pi\epsilon r}\right)R-AR=0, \quad (2.17)$$

$$\frac{1}{\sin\theta}\frac{\partial}{\partial\theta}\left(\sin\theta\frac{\partial Y}{\partial\theta}\right)+\frac{1}{\sin^2\theta}\frac{\partial^2 Y}{\partial\phi^2}+AY=0, \quad (2.18)$$

where A is the separation constant. Further separation of the angular equation is possible such that $Y(\theta,\phi)=\Theta(\theta)\Phi(\phi)$ giving,

$$\frac{\sin\theta}{\Theta}\frac{\mathrm{d}}{\mathrm{d}\theta}\left(\sin\theta\frac{\mathrm{d}\Theta}{\mathrm{d}\theta}\right)+\frac{1}{\Phi}\frac{\mathrm{d}^2\Phi}{\mathrm{d}\phi^2}+A\sin^2\theta=0. \quad (2.19)$$

Separating out the polar and azimuth equations, the system of equations becomes,

$$\frac{\mathrm{d}}{\mathrm{d}r}\left(r^2\frac{\mathrm{d}R}{\mathrm{d}r}\right)+\frac{2\mu r^2}{\hbar^2}\left(E+\frac{e^2}{4\pi\epsilon r}\right)R-AR=0, \quad (2.20)$$

$$\frac{\sin\theta}{\Theta}\frac{\mathrm{d}}{\mathrm{d}\theta}\left(\sin\theta\frac{\mathrm{d}\Theta}{\mathrm{d}\theta}\right)+A\sin^2\theta-B=0, \quad (2.21)$$

$$\frac{\mathrm{d}^2\Phi}{\mathrm{d}\phi^2}+B\Phi=0, \quad (2.22)$$

where B is another separation constant. Starting with the azimuth equation in Eq (2.22), solution of the form $C_1e^{im\phi}+C_2e^{-im\phi}$ where $B=m^2$ is obvious. The domain of ϕ is bound from 0 to 2π, thus m must be an integer. Choosing $C_2=0$, the solution takes on the form,

$$\Phi(\phi)=Ce^{im\phi},\quad m=0,\pm1,\pm2,\ldots \quad (2.23)$$

Updating the polar equation from Eq (2.21),

$$\frac{1}{\sin\theta}\frac{\mathrm{d}}{\mathrm{d}\theta}\left(\sin\theta\frac{\mathrm{d}\Theta}{\mathrm{d}\theta}\right)+\left(A-\frac{m^2}{\sin^2\theta}\right)\Theta=0 \tag{2.24}$$

Using a change of variables, $x=\cos(\theta)$, $P(\cos(\theta))=\Theta(\theta)$, and $\sin^2\theta=1-\cos^2\theta=1-x^2$, the polar equation becomes,

$$\frac{\mathrm{d}}{\mathrm{d}x}\left(\sin^2\theta\frac{\mathrm{d}P}{\mathrm{d}x}\right)+\left(A-\frac{m^2}{\sin^2\theta}\right)P=0 \tag{2.25}$$

$$(1-x^2)\frac{\mathrm{d}^2P}{\mathrm{d}x^2}-2x\frac{\mathrm{d}P}{\mathrm{d}x}+\left(A-\frac{m^2}{1-x^2}\right)P=0. \tag{2.26}$$

The remaining differential equation is of the Sturm-Liouville form with solutions known as the associated Legendre polynomials where,[65]

$$P_l^m(x)=(1-x^2)^{m/2}\left(C_0\sum_{j=0}^{\infty}\frac{C_{2j}}{C_0}x^{2j}+C_1\sum_{j=1}^{\infty}\frac{C_{2j+1}}{C_1}x^{2j+1}\right) \tag{2.27}$$

with the recursion relation,

$$\frac{C_{j+2}}{C_j}=\frac{(j+m)(j+m+1)-A}{(j+1)(j+2)}. \tag{2.28}$$

The above series converges asymptotically when $A=l(l+1)$ and $l=0,\pm1,\pm2,\ldots$. Coefficients C_1 and C_2 are dependent on l to force convergence of one of the series and killing off the other. Also, convergence criteria limits the allowed integral values of m such that $-l\geq m\geq l$ for each value of l. Note, the ground state value of $P_0^0(x)=1$.

After normalization, the angular wavefunctions, $Y_l^m(\theta,\phi)$, are referred to as spherical harmonics and can now be written as,

$$Y_l^m(\theta,\phi)=\kappa\sqrt{\frac{(2l+l)}{4\pi}\frac{(l-|m|)!}{(l+|m|)!}}e^{im\phi}P_l^m(\cos\theta)\quad\text{where}\quad\begin{cases}\kappa=(-1)^m & m\geq 0\\ \kappa=1 & m\leq 0\end{cases} \tag{2.29}$$

Substituting in A, the radial equation from Eq (2.20) becomes,

$$\frac{\mathrm{d}}{\mathrm{d}r}\left(r^2\frac{\mathrm{d}R}{\mathrm{d}r}\right)+\frac{2\mu r^2}{\hbar^2}\left(E+\frac{e^2}{4\pi\epsilon r}\right)R-l(l+1)R=0 \tag{2.30}$$

which can be rewritten as,

$$-\frac{\hbar^2}{2\mu}\left(\frac{\partial^2}{\partial r^2}+\frac{2}{r}\frac{\partial}{\partial r}-\frac{l(l+1)}{r^2}\right)R=(E-V)R \tag{2.31}$$

where V is the Coulombic potential. Letting,

$$u(r)\equiv rR(r),\qquad k\equiv\sqrt{-2\mu E/\hbar^2},\qquad \rho\equiv kr,\quad \text{and}\quad \rho_0\equiv\frac{\mu e^2}{2\pi\epsilon\hbar^2 k}, \tag{2.32}$$

(where $E<0$), the expression becomes,

$$\frac{\partial^2 u}{\partial\rho^2}=\left(1-\frac{\rho_0}{\rho}+\frac{l(l+1)}{\rho^2}\right)u. \tag{2.33}$$

As is well-documented, the solution can be given as,[66]

$$R_{n,l}(r)=\frac{1}{r}\rho^{l+1}e^{-\rho}\nu(\rho) \tag{2.34}$$

where,

$$\nu(\rho)=\sum_{j=0}^{j_{\max}}C_j\rho^j\quad\text{with}\quad\frac{C_{j+1}}{C_j}=\frac{2(j+l+1)-\rho_0}{(j+1)(j+2l+2)}. \tag{2.35}$$

Note, ν is a truncated asymptotic series that can be written as a polynomial of order $j_{\max}$ known as the associated Laguerre polynomials, $\nu(\rho)=L^{2l+1}_{n-l-1}(2\rho)$, with ground state $L^1_0=1$. The numerator of the recursion relation must vanish at $j_{\max}$. Defining the 'principle quantum number', $n\equiv j_{\max}+l+1$, we find $\rho_0=2n$.

In total, the final solution is,

$$\psi_{nlm}(r,\theta,\phi) = R(r)\Phi(\phi)\Theta\theta = NR_{n,l}(r)e^{im\phi}P_l^m(cos\theta), \tag{2.36}$$

with ground state,

$$\psi_{100}(r,\theta,\phi) = \frac{1}{\sqrt{\pi a_B^3}}\, e^{-r/a_B}, \tag{2.37}$$

where N is the overall normalization constant and l, m, and n are the so-called angular, magnetic, and principle quantum numbers, respectively. Thus, the discrete nature of the excitons can readily be seen as a direct consequence of the integral nature of the quantum numbers.

Most importantly, from the earlier definition of ρ_0 in Eq (2.32), the exciton Bohr radius can be defined as,

$$a_{_B} = \frac{4\pi\epsilon\hbar^2}{\mu e^2}. \tag{2.38}$$

Similarly the exciton binding energy $E_{_B}$ can now be determined,

$$E_{_B}^n = -\frac{\mu}{2n^2\hbar^2}\left(\frac{e^2}{4\pi\epsilon}\right)^2 = -\frac{e^2}{8\pi\epsilon a_{_B} n^2} = \frac{E_{_B}^1}{n^2} \qquad n = 1, 2, 3, \ldots \tag{2.39}$$

Taking rough semiconductor values of $\mu = .1$ and $\epsilon = 10$, the ground state value ($n = 1$) is $E_{_B}^1 = -13.6$ meV, known as the 'modified Ryberg' due to its striking similarity to the hydrogen atom. Note, there is no **k** dependence in this result.

2.3.2 Quantum Dot as Spherical Potential Well

A semiconductor QD can be elementarily modeled as a spherical potential well using three main assumptions:[3,58,67,68]

1. The QD is perfectly spherical with radius a.

2. The interior of the QD is a reciprocal and uniform medium.

3. The potential energy at the surface of the QD is infinite.

The Hamiltonian for such a system is simply the sum of the kinetic and potential energies such that,

$$\mathcal{H} = T_k + V = \frac{\hbar^2}{2\mu}\nabla^2 + V(r), \qquad V = \begin{cases} 0 & r \leq a \\ \\ \infty & r \geq a \end{cases} \tag{2.40}$$

where r is the radial distance from the center of the QD and, again, replacing the classical mass with the reduced effective mass μ within the EMA framework. Solving the Schrödinger equation for the system, the equation takes the familiar form of a radial equation, though simplified by the zero potential within the QD,

$$\frac{\partial^2 u}{\partial r^2} = \left(\frac{l(l+1)}{r^2} - k^2\right)u \tag{2.41}$$

where the $l(l+1)$ term comes from the separation constant of the polar equation. Recall, $u \equiv rR(r)$ and $k \equiv \sqrt{2\mu E/\hbar^2}$. The quantized energy state solution of a spherical quantum dot of radius a for electrons and holes is given by,

$$E_{n,l} = \frac{\beta_{n,l}^2 \hbar^2}{2\mu a^2}, \tag{2.42}$$

where $\beta_{n,l}$ is the n^{th} zero of the l^{th} spherical Bessel function with ground state $\beta_{1,0} = \pi$. This result shows a straightforward qualitative dependence of the energy levels the size of the dot is confined, the energy levels increase as $1/a^2$.

2.3.3 Confinement Effects on Light Emission and Absorption Characteristics

Given a QD of radius 'a' and modeling it as a spherical potential well, the solutions of the exciton binding energies and the confinement energies were derived. Substituting the

appropriate terms, the transition energy $\hbar\omega$ is,

$$\hbar\omega = E_g + E_B^n + E_{n,l} = E_g - \frac{e^2}{8\pi\epsilon a_{_B} n^2} + \frac{\beta_{n,l}^2 \hbar^2}{2\mu a^2}. \tag{2.43}$$

Considering the ground state solution ($n = 1$), we find,

$$\hbar\omega = E_g - \frac{e^2}{8\pi\epsilon a_{_B}} + \frac{\pi^2 \hbar^2}{2\mu a^2}. \tag{2.44}$$

When the quantum dot radius is on the same order or smaller than the exciton Bohr radius $a_{_B}$, the Brus formalism shows that the ground state becomes,[40]

$$\hbar\omega = E_g - 1.8\frac{e^2}{4\pi\epsilon a} + \frac{\pi^2 \hbar^2}{2\mu a^2}, \quad \text{where} \quad a_{_B} \approx \frac{a}{1.8} \tag{2.45}$$

where the exciton binding energy is calculated in first order perturbation theory. By making the diameter of a quantum dot smaller, we can raise the kinetic energy as $\sim 1/a^2$, which has the effect of broadening the separation of energy states. As a decreases, there is increased separation of the discrete valence and conduction energy levels, lending to a blue-shift of the absorption and emission spectra. The Coulombic potential goes as $\sim 1/a$, offsetting the confinement effects slightly. The increased attraction can be envisioned as increased overlap of the electron and hole wavefunctions, lending to higher radiative recombination probability and oscillator strength in smaller QDs. We now can see a clear dependence of size while operating within the strong confinement regime.

The discrete ground energy states in the QD conduction and valence bands are known as the lowest unoccupied molecular orbit (LUMO) and highest occupied molecular orbit (HOMO). Transitions will always occur between associated energy levels of the same quantum number n. Importantly, recombinations lead to the emission of a photon whose wavelength is related to the energy gap between charge carriers prior to recombination. Thus, the size, temperature, purity (crystallinity), and crystalline phase & composition of the material all play into recombination properties.

Chapter 3

Methods of Processing Quantum Dots with Isopropyl Alcohol

Though the colloidal production of such nanoparticles was not performed in this study, the pathway of colloidal synthesis has become mainstream due to the fast, low-cost, high-quality synthesis of crystalline QDs. Highly-luminescent, ∼6 nm diameter $CdSe_{0.83}S_{0.17}$/ZnS core-shell QDs suspended in toluene (∼1 mg/mL) were obtained commercially (Sigma Aldrich). The QDs are extremely vibrant when illuminated by UV excitation of 365 nm. Exploiting the solution processability of colloidal QDs, a set of treatment methods were developed simply utilizing drop-cast QDs on glass slides and exposing them to isopropyl alcohol in various apparatus configurations.

3.1 Introduction

Colloidal QDs can be exposed to a solution, allowing full surface exposure, unlike dry etching. Generally speaking, wet etching utilizes solution-based (liquid-phase) etchants that remove material in three distinct steps:

1. The reagents contact the surface via solution.

2. The reagents react with the surface.

3. The byproducts of the reaction move away from surface.

Wet etching offers selectivity of many solutions and etchants for materials, some of which are well-documented. However, the reaction rate and crystal face selectivity (anisotropy) of the etchant and surface must be well-suited for the nanoscale application to QDs. Additionally, variations in etchant concentration, temperature, and exposure time complicate results. Ideally, reduction of colloidal QD size would bare no influence on shape, composition, or crystallinity of the QD in order to maintain the highly luminescent behavior associated with excitonic emission. Many of the solutions given in such texts are strong acids or bases, such as hydrofluoric and sulfuric acids, that tout high reaction rates that would destroy the QDs used in this study.[69]

Cadmium and zinc based semiconductors (CdSe, CdS, and ZnS in this case) can be dissolved by photo-oxidation of the chalcogenides in aqueous suspension.[70] Successful oxidation results in Cd^{2+} and Zn^{2+} which both form soluble coordination compounds. In an effort to form novel controllable wet etching strategy with the II-VI semiconductors, a mild isopropyl alcohol and water mix were used to reduce the size of as-grown core-shell QDs per the methods outlined below.

The main method developed herein makes use of a horn sonicator to expose QDs to solution. The use of horn sonication fulfills two symbiotic purposes. First, the dissipation of ultrasonic (acoustic) energy results increased solution temperature. This temperature is easily monitored via thermal probe and can be indirectly controlled by setting the output power. With increasing temperature, the chemical process will accelerate. Though this is desirable from the standpoint of potential viability of the method, it was important to maintain consistent solution concentrations throughout processing intervals. Therefore, temperatures below the evaporation point of isopropyl alcohol, which has an atmospheric boiling point of 82.5°C, were targeted. In this case, setting the sonicator output power to ∼9 W was sufficient to increase the solution to ∼60°C. The temperature was monitored and routinely stabilized around 30 seconds of processing starting with an alcohol solution at room temperature. Second, sonication provides sufficient kinetic energy to overcome the

surface tension of the solution thereby creating an aerosol above the liquid boundary. This novel etching method allows the QDs to interface with solution in multiple phases while being exposed simultaneously to atmosphere.*

3.2 Vapor-Based 'Sonication' Treatment Method

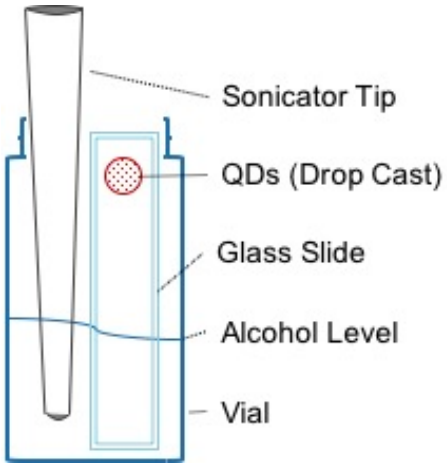

Figure 3-1: Schematic of vapor-based treatment. CdSeS alloyed QDs are drop-cast onto a slide and suspended within a vial while the solution is sonicated. The sonicator acts as a heat source and exposes the QDs to a vapor/mist blend.

As a first step, a 1μL aliquot of QDs is drop-cast onto a glass slide. Once the toluene evaporates (∼3–4 min.), the slide is fitted vertically into a vial containing ∼25mL of C_3H_8O:H_2O 10:1 solution with QDs located ∼1 cm above the liquid/air interface.

The solution is agitated and simultaneously heated ultrasonically with a horn sonicator (Misonix 3000, ∼9 W, ∼54°C). The QD samples were next exposed to the etchant mist/vapors by sequentially increasing etch time by 3 mins for up to 15 minutes. The slide was taken out at the end of each 3 min treatment, allowing the same sub-area of the sample to be optically analyzed using photoluminescence (PL) emission measurements, the results of which are discussed in more detail in the next chapter.†

*QDs were exposed explicitly to vapors by suspension above boiling solution as well as submerged in room-temperature solution. The vapor-only and liquid-only treatment did not exhibit any visible emission shifting after hours of processing.

†All processing treatment methods were optically monitored using a handheld UV lamp with a constant wavelength of $\lambda \sim 365$nm. Though the lamp proved useful for easy monitoring the state of processing, the methods were also rerun for the same time periods in low-light conditions giving similar results in each

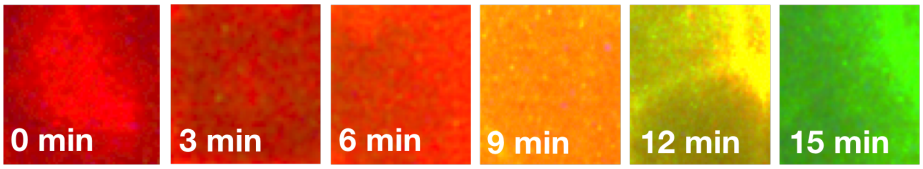

Figure 3-2: Optical microscope images (∼100X) of drop-cast $CdSe_{1-x}S_x$/ZnS QDs processed with 91% C_3H_8O water solution at varying durations captured with an in-microscope camera; the samples were excited with a UV light. $\lambda_{exc.}$= 365 nm

The emission QDs treated with the 10:1 mixture of isopropyl to DI water demonstrated a consistent blue-shift with the exposure time, shifting visibly from red to green over the course of 15 mins of treatment, shown in Figure 3-2. Treatments carried out with only with pure DI water or ∼99.9% C_3H_8O had no impact on the emission characteristics. However, for exposure time greater than 15 minutes, samples treated with ∼99.9% C_3H_8O resulted in noticeable loss of luminescence yield.

3.3 Liquid-Phase 'Droplet' Treatment Method

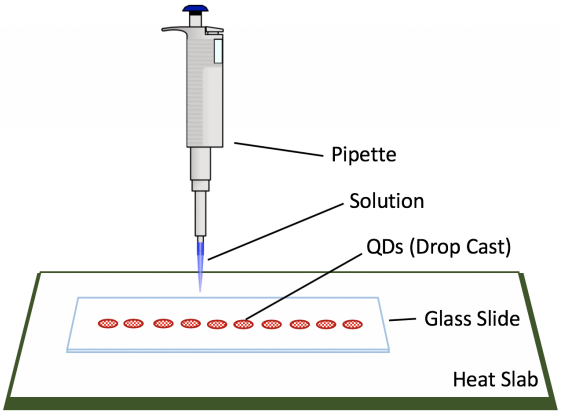

Figure 3-3: Schematic of liquid-phase 'droplet' treatment method. A hand-held pipette or burette (not shown) was used to drop solution directly onto QD samples.

Alternative treatments were carried out in a liquid-phase by drop-casting 91% alcohol solution directly onto drop-cast QD samples via burette or hand-held pipette. By adjusting the burette valve, a relatively consistent rate of droplets (∼3–5/min) could be applied to

case.

a sample for prolonged periods of time, $>$ 2hr. The applied solution was allowed to completely evaporate prior to reapplication of a new droplet. This exposed the QDs to solution in liquid-phase and vapor-phase in addition to the atmosphere.

The QDs were slightly heated with an external electrical heat source to maintain similar temperatures to those measured during sonication for direct comparison ($\sim$60°). While the trends (color evolution) were similar to those described earlier, the alternative pathway is generally found to be an order of magnitude slower compared to the sonication method, taking several hours to exhibit a partial shift in emission color by comparison. This is attributed to a strong dependence of the etch rate on the sample temperature and exposure to atmosphere, which was generally higher for the vapor-phase, i.e. sonication-based method. As samples treated using both approaches exhibited similar characteristics, the characterization and analysis of the effect of the alcohol etching on the structural and optical properties of QDs is limited to samples obtained from the first method.

Chapter 4

Characterization Methods

To characterize properties of the 'as-grown' $CdSe_{0.83}S_{0.17}$/ZnS QDs both prior to and following alcohol processing via sonication method, various characterization techniques are used and cross-analyzed.* The acquired data sets from the following characterization methods are treated individually in this chapter, but it should be stressed that the selection of these methods is rooted in the anticipated consequences within our theoretical framework, per Chapter 2. In particular, the size evolution of QDs is shown to theoretically determine the evolution of the optoelectronic behavior. Ideally, a single technique that allows measurement of geometrical, structural, compositional, and optoelectronic properties would be used simultaneously to show purely correlative data sets. However, an ideal type of measurement apparatus that achieves an 'all-in-one' result was not available to the author, nor is it believed generally that such an apparatus exists. Therefore, numerous samples and characterization techniques were used in tandem to define the evolution of the aforementioned properties of QDs as a function of processing time.

This chapter outlines the basic principles behind selected characterization techniques and their general results. Results are contrasted against theoretical QD treatments more thoroughly in the next chapter.

*EDX evaluation completed with help from Elaheh Kheirandish and Dr. Heather Owen at UW-Milwaukee's Biological Sciences Microscopy and Imaging laboratory, equipped with a Hitachi S-4800 FE-SEM microscope with Bruker Quantax EDS system. Using mapping analysis, the the QD core alloy ratio of selenium to sulfur was found using atomic percentages assuming a 1:1 Zn:S ratio for the shell.

4.1 High Resolution Transmission Electron Microscopy

Over the course of processing, an emission blue-shift was observed. The QDs are suspected to decrease in size as a function of processing time, per the theory. Therefore, obtaining the size and shape distributions of QD samples are of interest to contrast to their emission properties. Additionally, the crystallinity and crystal structure states of processed and as-grown $CdSe_{0.83}S_{0.17}$/ZnS QD samples are needed to confirm processing morphology effects. As discussed earlier, cadmium selenide, cadmium sulfide, and their alloys are II-VI semiconductors with a natural crystalline phase of hexagonal (wurtzite) structure. The associated lattice constants of these structures have been reported on the order of $\sim$.5 Å. Thus, an imaging mechanism by which such structures can be resolved is needed.

4.1.1 Electron Microscopy Principles

Due to diffraction and interference phenomena, imaging systems making use of particles that exhibit wave-like properties (e.g. photons and electrons) are limited in resolution due to the formation of an Airy disc. In a perfect optical system, resolution d (minimum discernible distance of two points) can be described by the Rayleigh criteria,

$$d = \frac{1.22\lambda}{2n\sin\theta} = 0.61\frac{\lambda}{\mathrm{NA}} \tag{4.1}$$

where λ is the 'particle' wavelength, n is the refraction index of the system, θ is the half angle exciting the lens/aperture, and NA is the numerical aperture. Other resolution conventions exist, such as the Abbe ($0.5\frac{\lambda}{\mathrm{NA}}$) and Sparrow ($0.47\frac{\lambda}{\mathrm{NA}}$) limits, but we'll continue with the Rayleigh limit here.

Consider the de Broglie wavelength of an electron of mass m and velocity v,

$$\lambda = \frac{h}{mv} \tag{4.2}$$

where h is the Planck constant. By altering the velocity of the electron, the electron

wavelength is inversely affected. Electron microscopy methods make use of this property by altering the electron velocity formed by a electrostatic potential V, where the electron kinetic energy eV is given by (neglecting relativistic effects),

$$eV = \frac{1}{2}mv^2. \tag{4.3}$$

where e is the static charge of the electron. This is synonymous to setting the kinetic energy of the electron by choosing the accelerating voltage V. Now,

$$\lambda = \frac{h}{mv} = \frac{h}{m\sqrt{2eV/m}} \approx \frac{12.25 \times 10^{-10}}{\sqrt{V}} \tag{4.4}$$

If we consider the relativistic effects, the result is multiplied by a $\left(1 + eV/2mc^2\right)^{-1/2}$ term. Therefore, for voltages of 100 keV, 200 keV, and 300 keV in electron microscopes, the wavelengths are 3.70 pm, 2.51 pm and 1.96 pm, respectively. Photon sources are limited in the gamma ray ($\lambda \sim 10^{-12}$ m) realm and therefore cannot match the resolutions shown below.

If we consider $n \approx 1$ and for small angle $\sin(\theta) \approx \theta \approx 10^{-2}$, the Rayleigh resolution limit becomes,

$$d = 0.61\frac{\lambda}{n \sin\theta} \approx 61 \cdot \lambda, \tag{4.5}$$

giving resolutions of 2.25 Å, 1.53 Å, and 1.12 Å for voltages of 100 keV, 200 keV, and 300 keV, respectively. In the practical case, aberrations and distortions determine the resolution, ~1 Å with current technology. This rather astounding imaging resolution empowers the sub-atomic imaging of crystalline structures such as QDs by way of electron microscopy.

Specifically, transmission electron microscopy (TEM) sufficiently accelerates a beam of electrons to propagate through a thin sample prepared typically on a small copper mesh grid.[71] The grids in this study were coated with a layer of carbon for better adsorption of QD samples onto the mesh surface. The mean free path of the electrons must be large enough to

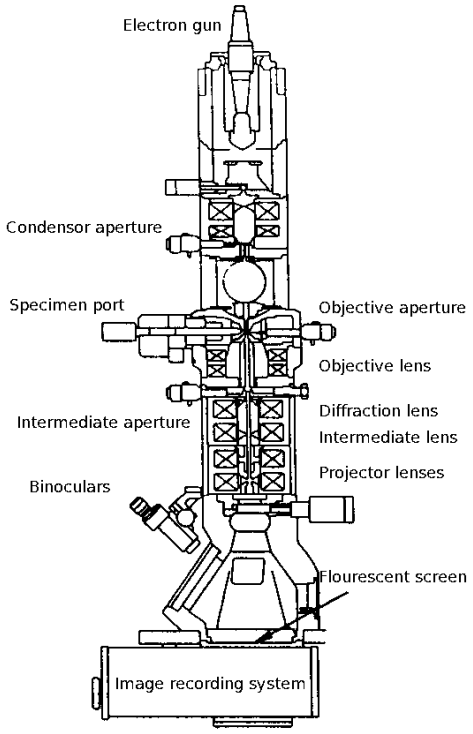

Figure 4-1: Diagram outlining the internal components of a basic TEM system.

mitigate unwanted scattering from impurities in the chamber, so the process needs to occur in ultra-high vacuum. The electron source supplies electrons which are formed into a beam using electromagnetic lenses. The beam of electrons interfaces with the atomic structure of the sample, which is comprised of electron-surrounded atoms. The repulsion of the electron beam and the atoms results in the scattering of propagating electrons. The accelerating voltage and composition of the material dictate the maximum thickness of the sample to ensure propagation, $<$ 100 nm at 100 keV is typical.

Propagating electrons are then sent through a set of lenses to form an image on a fluorescent screen. Contrast is generated either by sample thickness variations or by the composition of the sample, where higher atomic number elements pose increased backscattering probability (diffraction contrast). Both create amplitude contrast in the final image. Non-scattered electrons generate a maximum fluorescence upon incidence with the screen, resulting in bright areas in the image. Conversely, backscattered electrons do not make it to the screen and no fluorescence occurs, resulting in dark areas in the image. Electron

phase differences can also be used to generate contrast in images. The use of both phase and amplitude contrast allows for the highest resolution of imaging and is often referred to as high resolution transmission electron microscopy (HRTEM). The resulting screen image can be optically viewed through a filter screen or with use of binoculars. Additionally, a charge-coupled device (CCD) can be used for digitally imaging.

For the case of a crystal, the regular and repeating lattice provides patterned contrast from its surroundings. The crystalline purity, as well as any defects, can be readily detected and distinguished. It turns out in this study, the crystal signature was absolutely paramount to determine the size and shape of each QD, as shown below.

A crystalline sample will also exhibit Bragg scattering. The diffraction pattern is dependent on sample orientation, so many specimen holders allow for rotational modification to properly align the sample for a given plane. The diffraction pattern can be imaged and gives insight into the crystallographic structure of the sample. Alternatively, the use of image processing can give similar insight into crystal structure. By taking the Fourier transform of a HRTEM image, the reciprocal space image is formed and can be analyzed to find the crystalline structure. This latter method creates a diffractogram, the analysis of which is presented for this study in the next chapter.

4.1.2 HRTEM of CdSeS Quantum Dots

QDs processed for 15 minutes in addition to unprocessed (as-grown) samples were sent to the UWM-HRTEM laboratory for preparation and evaluation.[†] Multiple as-grown and processed samples were imaged to allow for statistical analysis of the collected images.

Figure 4-2 shows two sample images of individual QDs. In both cases, the as-grown (a) and processed (b) QDs exhibit regular and repeating contrast structure associated with crystal structure.

[†]Specimen preparation and HRTEM evaluation completed with help from Elaheh Kheirandish and Dr. Marvin Schofield at UW-Milwaukee's HRTEM laboratory, equipped with a Hitachi H-9000NAR microscope.

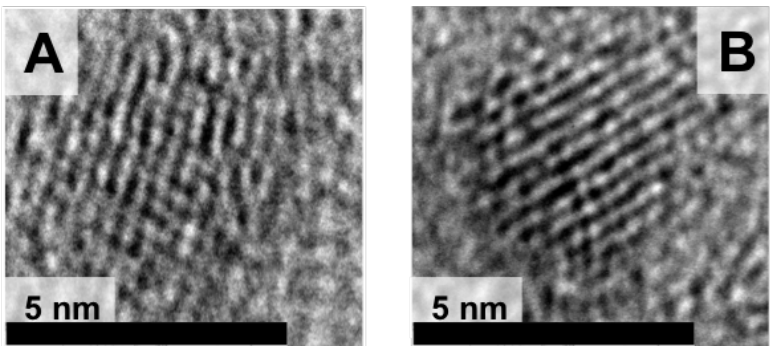

Figure 4-2: Sample QD images captured during HRTEM. In both cases, the as-grown (a) and processed (b) QDs exhibit crystallinity while the surrounding area does not.

Making use of ImageJ software, size and shape of the areas encompassed by individual QDs were determined by tracing the patterned edge of each crystalline region. Only QDs whose crystalline centers were in focus were used for analysis. Larger area examples are shown in Figures 4-3. Statistical analysis of the sizes and shapes were obtained for both as-grown and processed QDs. The calculated values are shown in Tables 4.1 and 4.2.

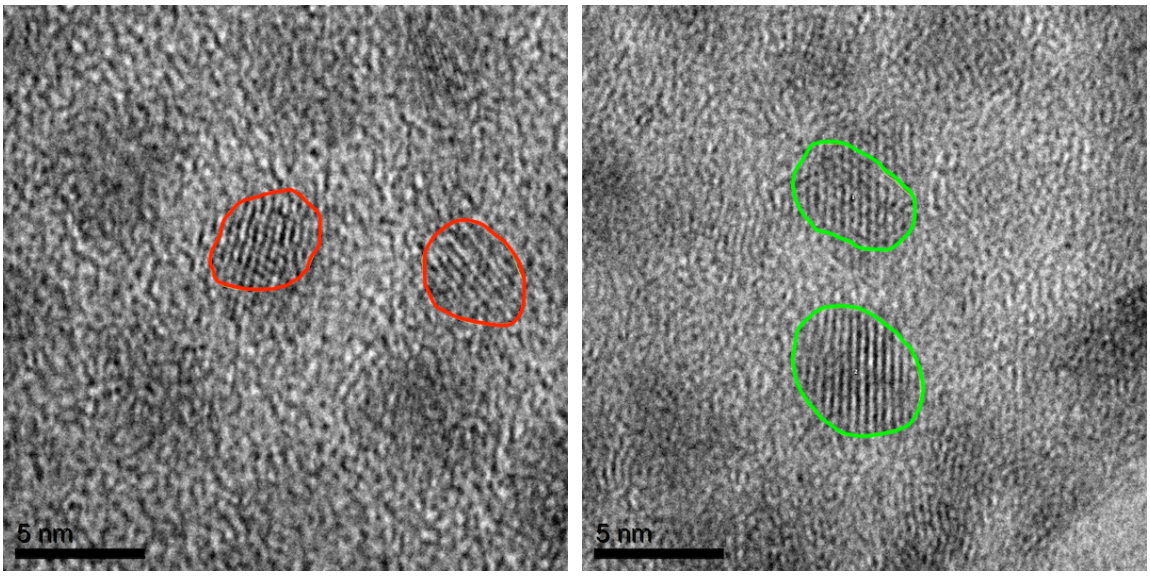

Figure 4-3: HRTEM image of as-grown (Left) and processed (Right) QDs. The crystalline regions are outlined and later statisically analyzed by ImageJ software. Note, the outlines shown are enhanced post analysis for easier viewing.

Table 4.1: Statistical results of HRTEM image analysis for **as-grown** $CdSe_{0.83}S_{0.17}$/ZnS QDs. The area, major axis, minor axis, and aspect ratio are shown.

	Area (nm^2)	Major (nm)	Minor (nm)	AR
Mean	27.0	6.7	5.1	1.3
StdDev	5.6	0.75	0.58	0.12
Min	12.7	4.3	3.3	1.1
Max	42.0	8.0	6.7	1.7

Table 4.2: Statistical results of HRTEM image analysis for **processed** $CdSe_{0.83}S_{0.17}$/ZnS QDs. The area, major axis, minor axis, and aspect ratio are shown. Processing time was for 15 minutes via sonication method.

	Area (nm^2)	Major (nm)	Minor (nm)	AR
Mean	14.6	4.7	3.8	1.2
StdDev	3.6	0.65	0.56	0.12
Min	4.7	2.7	2.2	1.0
Max	25.1	6.1	5.2	1.5

4.2 Photoluminescence Spectroscopy

4.2.1 Review of Photoluminescence Spectroscopy

Photoluminescence spectroscopy (PL) is a non-destructive method used for characterizing the optical properties of materials.[71,71,72] PL results offer information about energy transition processes, particularly in solid-state materials. An optically absorbing solid will create an electron-hole pair given an incident photon of sufficient energy. The electron is promoted from the valence band to the conduction band leaving a positive region, or 'hole', where it once resided. During recombination of the electron-hole pair, a photon is emitted. The spontaneous emission of light through this process is called photoluminescence. Thus, the excited state properties of a material can be can be characterized by its recombination emission spectra.

Conceptually, the transition energy, or the energy difference between lowest unoccupied molecular orbital (LUMO) and highest occupied molecular orbital (HOMO) states, corresponds to the conduction and valence band edges, respectively. Recombinations at this transition energy are prevalent in a pure crystal and result in emission spectra localized at this energy. However, impurities, defects, and trap sites provide energy levels within

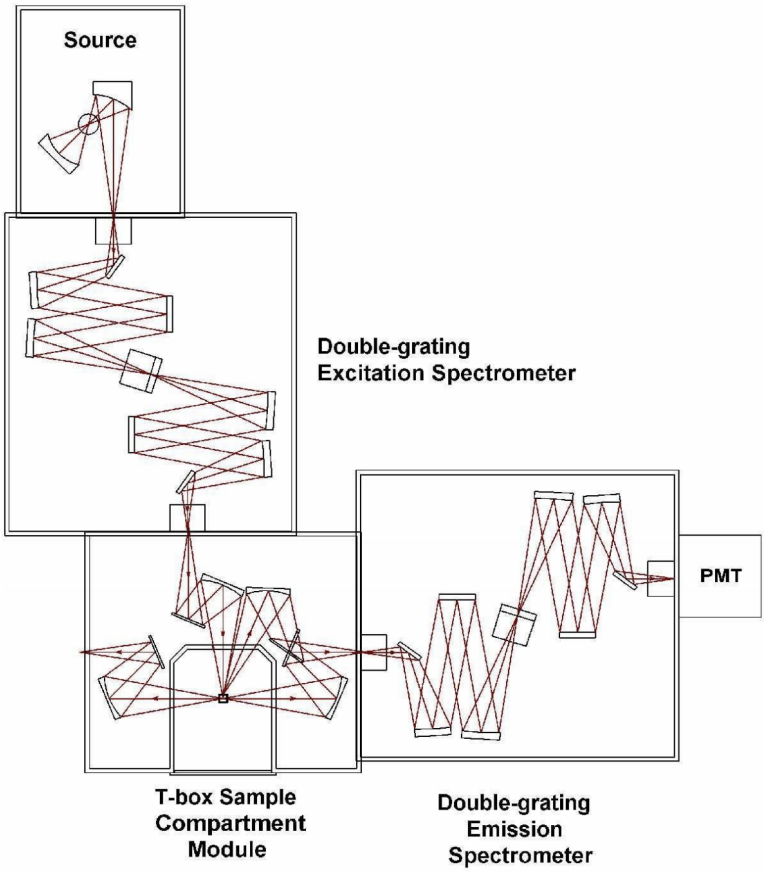

Figure 4-4: Schematic of Fluorolog FL3-22 PL system, incorporating double-grating spectrometers in both the excitation and emission positions for high resolution, sensitivity, and stray-light rejection. *Reprinted with permission from HORIBA, Ltd.*[73]

the band gap of the idealized material. Recombinations occurring from these sites are detectable in PL, resulting in the presence of lower energies (or longer wavelengths) in the PL spectra. Therefore, the transition energy and quality of a material can be qualitatively monitored using PL techniques.

Generally speaking, PL systems require: (a) stable and selectable monochromatic light source, (b) sufficient optics as to focus the light on a sample, (c) stage on which to affix the sample, (d) collection optics and emission monochromator, and (e) detection mechanism. The PL system used in this experiment is schematically depicted in Figure 4-4.[73] The system utilizes a 450 W xenon lamp as the excitation source ($\sim$5 mW/cm^2) that is filtered with a double-grating monochromator (DGM). The monochromatic radiation is fed into the sample through an Olympus 51x microscope (not pictured). The detected emission

from the sample is filtered through a second DGM and is detected by a photomultiplier tube (PMT) in photon counting mode. The spectra obtained provide a means to determine emission parameters such as peak symmetry, full width half max (FWHM) of the peak(s), and center position of the peak(s) through decompositional fitting of multiple Gaussian or Lorentzian curves using analysis software, such as Origin or SciDavis.

4.2.2 cw-PL of CdSeS Core-Shell Quantum Dots

In these studies, constant wavelength photoluminescence (cw-PL) was employed, setting the wavelength of the excitation source in UV (λ_{exc} = 365 nm) for all data acquisitions. $CdSe_{0.83}S_{0.17}$/ZnS QD samples sequentially processed by 10:1 isopropanol:water via sonication method were analyzed using cw-PL emission measurements.[‡] The emission of samples were spectrally analyzed from ∼380 - 700 nm with an acquisition time of 2 sec/nm. To maximize consistency between processing time interval data sets, the sample was monitored via CCD camera and aligned on the PL microscope stage by targeting visible density variation signatures in the drop-cast QDs. This allowed analysis of roughly the same sub-area of a single sample as it progressed through processing intervals.

The raw cw-PL spectra data was smoothed using adjacent point averaging (5 points) to reduce the noise-like variations present on the raw spectral data. Each of the cw-PL data sets were decoupled from the PL background using a multi-peak fitting tool within SciDavis open-source software. Figure 4-5 shows the resulting cw-PL spectra acquired for as-grown and processed QDs via sonication method for intervals of 3 minutes. Though as-grown QDs possess a single excitonic emission peak, processed QDs show multiple peaks. The fitting of 3 Gaussian distributions generated consistent results for processed samples, with accuracy values (fitted variation / total variation) of $R^2 > 99\%$. A fitting example is shown in Figure 4-6 for QDs processed for 9 minutes. In this fitting scheme, a dominant peak migrates from ∼626 nm (red) to ∼545 nm (green) with two additional peaks located relatively near ∼556 nm and ∼500 nm, Table 4.3.

[‡]cw-PL measurements and equipment setup performed by Elaheh Kheirandish in Prof. Nikolai Kouklin's laboratory, equipped with a Fluorolog® FL3-22.

Table 4.3: Data extracted from cw-PL (λ=365 nm) emission spectroscopy curves for $CdSe_{0.83}S_{0.17}$/Zn QDs processed via sonication method in 3-minute time intervals (P.Time). The processed curves were fitted using 3 Gaussian peaks, example shown in Figure 4-6. The as-grown QDs only exhibits one excitonic peak. Peak # is determined by decreasing order of center values.

P. Time (min)	**Peak #**	**Area**	**Center** (nm)	**Width** (nm)	**Height** (a.u)	**FWHM** (nm)
as-grown	1	503,103.0	626.5	27.1	14794.1	63.8
3	1	10,696.2	604.7	32.4	263.0	76.2
	2	12,611.1	560.7	66.3	151.7	155.9
	3	5,865.4	495.6	39.5	118.5	92.8
6	1	15,743.2	598.5	31.2	402.1	73.4
	2	13,063.7	566.3	52.2	199.6	122.7
	3	7,709.7	500.8	46.4	132.6	109.0
9	1	13,879.7	592.2	31.8	348.4	74.7
	2	18,095.6	564.5	55.9	258.3	131.4
	3	7,226.3	500.1	43.9	131.3	103.2
12	1	9,968.1	579.2	40.7	195.6	95.6
	2	2,935.3	545.6	29.3	80.0	68.8
	3	10,822.1	502.2	60.9	141.7	143.2
15	1	9,246.4	545.8	72.1	102.3	169.4
	2	943.3	543.4	23.2	32.4	54.6
	3	6,170.6	500.3	41.0	120.0	96.4

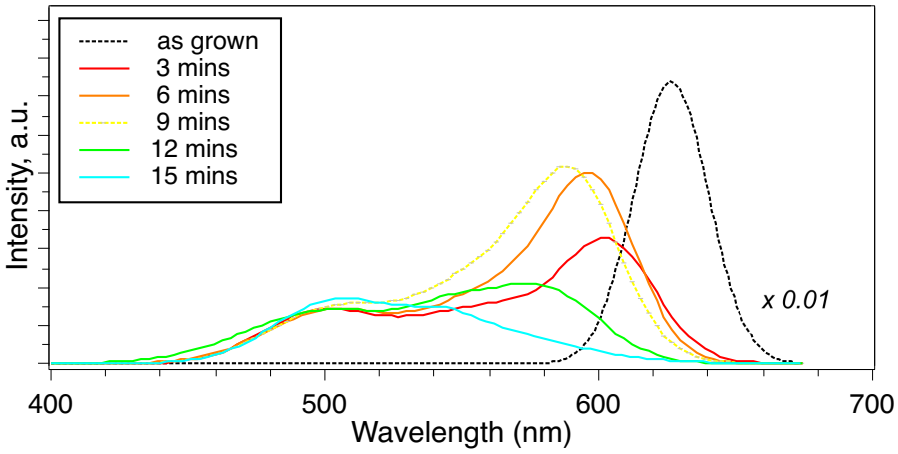

Figure 4-5: cw-PL emission results for CdSeS/ZnS QDs processed via sonication method in 3-minute intervals. The as-grown QDs exhibit a single excitonic peak whereas the processed samples exhibit multiple peaks. $\lambda_{exc.} = 365$ nm

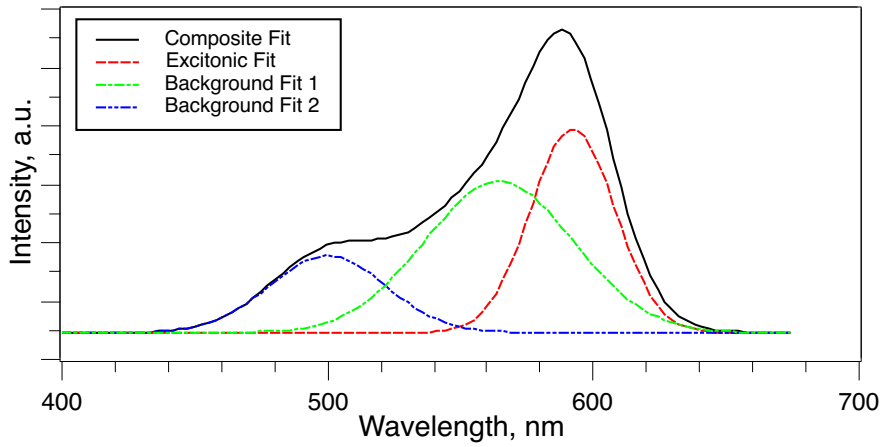

Figure 4-6: Gaussian multi-peak fitting of QDs processed via sonication method for 9 minutes, as example. The lowest energy peak is attributed to QD excitonic emission. The remaining peaks are attributed to background emission. $\lambda_{exc.} = 365$ nm

By decomposing each PL data set into 3 distinct Gaussians curves, the evolution of individual recombination pathways throughout processing can be analyzed. Figure 4-7 shows the upper-most (longest peak wavelength) Gaussian for each processing duration. This emission is attributed to the excitonic emission of the QDs, demonstrating a color shift consistent with visual results, shown in Figure 3-2.

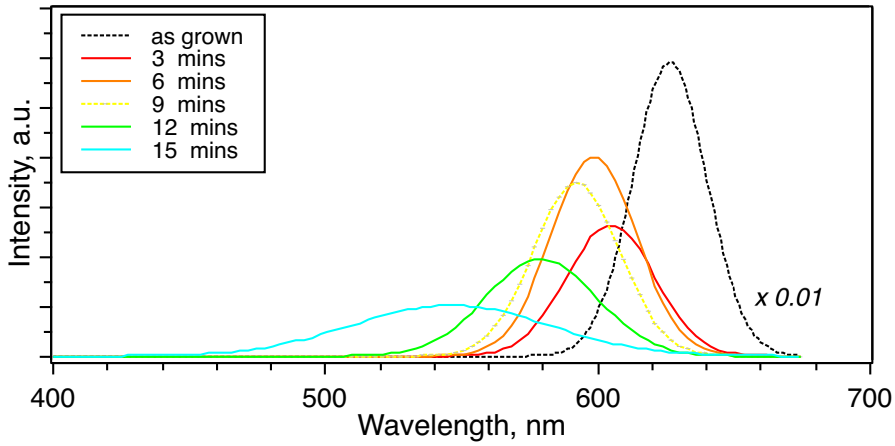

Figure 4-7: Excitonic emission of as-grown and processed QDs via sonication method in 3-minute intervals. Emission peaks consistently migrate to higher energy wavelengths with processing time. $\lambda_{exc.} = 365$ nm

Table 4.4: Statistical average (mean) and standard deviation (Δ) values of processed QD samples (3-15 minutes) derived from Table 4.3.

Peak	**Center** (nm)	Δ	**Height** (a.u.)	Δ	**FWHM** (nm)	Δ
1	584.1	23.4	262.3	119.3	169.4	41.0
2	556.1	10.8	144.4	90.5	155.9	43.1
3	499.8	2.5	128.8	9.6	143.2	20.2

Table 4.5: Ratio of excitonic integrated emission to net-PL (total integrated emission) of as-grown and processed QDs in 3-minute intervals. Derived from Table 4.3.

Time (min.)	**Total Area**	**Excitonic Area**	**Ratio**
as-grown	503,103.0	503,103.0	1.00
3	29,173	10,696	0.37
6	36,517	15,743	0.43
9	39,202	13,880	0.35
12	23,726	9,968	0.42
15	16,360	9,246	0.57

Chapter 5

Analysis of the spectroscopic data: EMA model

5.1 Analysis of HRTEM Data

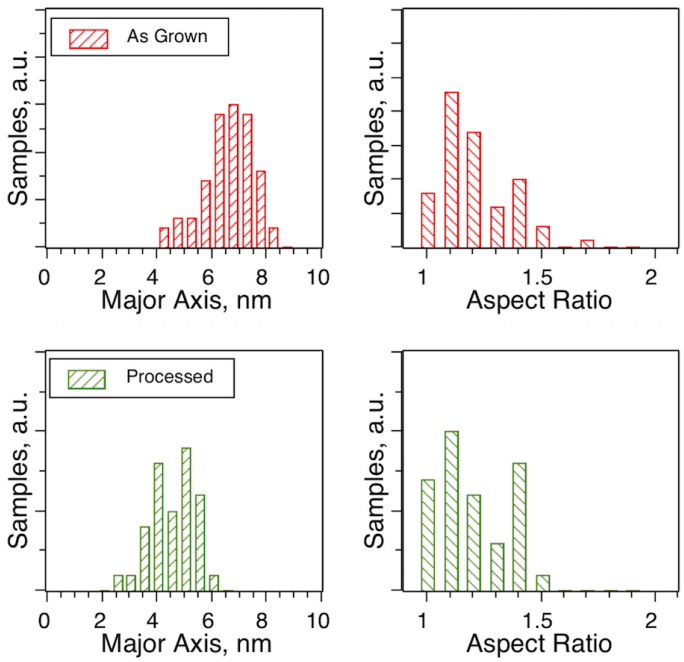

Figure 5-1: Statistical distributions of major axis diameter and aspect ratio of as-grown and processed $CdSe_{0.83}S_{0.17}$/ZnS QDs plotted as histograms. The major diameter (Left) for and aspect ratio (Right) distributions of QDs before (Top) and after processing (Bottom) for 15 min via sonication method. Statistical mean, range, and processing induced change values shown in Table 5.1.

Table 5.1: Statistical mean, range, and change values obtained from HRTEM images for as-grown and QDs processed for 15 minutes, supplementary to histograms plotted in Figure 5-1.

		As-grown	Processed	Change
Major Diameter	Mean (nm)	6.65	4.74	1.91
	Range (nm,%)	3.79	3.39	10%
Aspect Ratio	Mean (nm)	1.31	1.25	0.06
	Range (nm,%)	0.50	0.59	18%

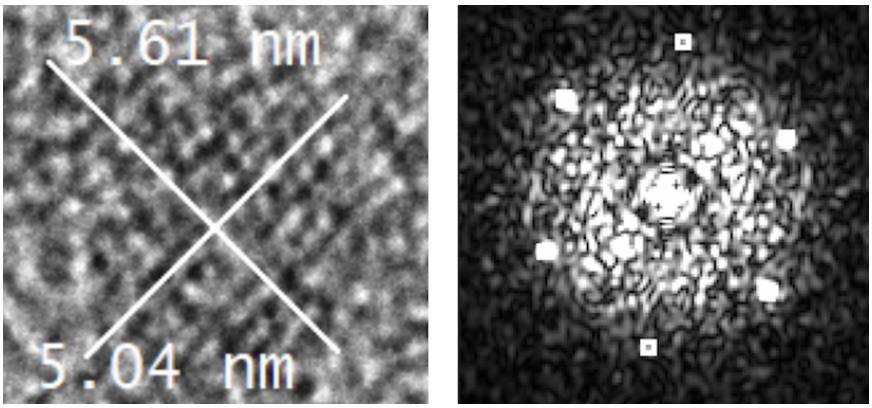

Figure 5-2: (Left) HRTEM image of single as-grown $CdSe_{0.83}S_{0.17}$/ZnS QD, with dimensions 5.61×5.04 nm^2 and lattice parameters $a = 4.1$ Å and $c = 6.7$ Å. (Right) Diffractogram of image on left showing the hexagonal structure with average angle of 60 $\pm 6.84°$.

HRTEM images of as-grown and processed $CdSe_{0.83}S_{0.17}$were collected to understand the impact of the alcohol processing on the diameter and aspect ratio distributions. These images contain QD ensembles, the shapes and sizes of which were determined though statistical analysis via image processing. The statistical distribution histograms are presented in Figure 5-1 with the corresponding mean values and ranges listed in Table 5.1. During processing the major diameter undergoes reduction of 1.91 nm while the diameter aspect ratio value undergoes only a slight change from 1.31 to 1.25. The distribution range is maintained for both parameters, confirming that the used alcohol-based processing is isotropic. As such, the etching rate of QD structures by alcohol in this context does not appear to be selective or dependent on crystal plane orientation at the surface. This result is substantial, as there has been no known reported method to isotropically down-tune such QDs without distorting the shape or destroying the crystallinity through more aggressive treatments.

HRTEM of the as-grown quantum dots matches with CdSeS hexagonal wurtzite struc-

ture with {100}, {002} and {101} planes.[74] The average lattice constants a and c of the as-grown quantum dots is 4.1 Å and 6.7 Å, respectively.* A single as-grown QD HRTEM and corresponding diffractogram are shown in Figures 5-2.

5.2 EMA Modeling of Excitonic PL Spectra

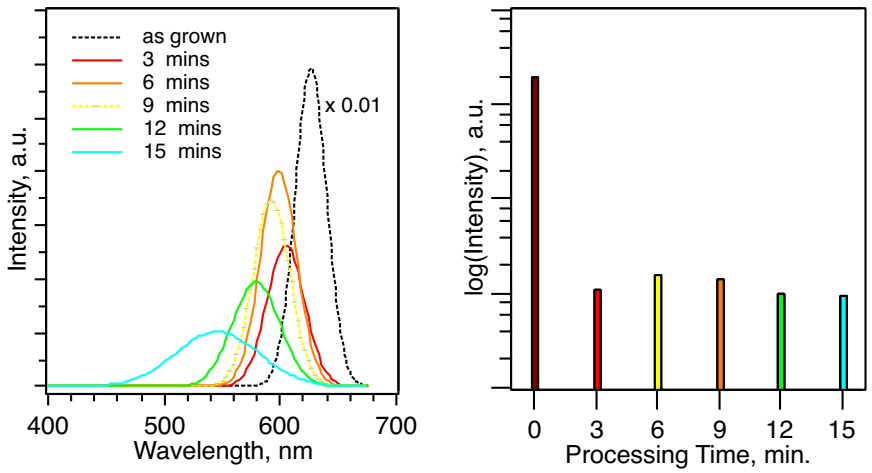

Figure 5-3: (a) Excitonic emission spectra of alcohol processed $CdSe_{0.83}S_{0.17}$/ZnS QDs in 3-min sonication intervals. (b) Semi-log plot of total integrated emission (net PL). After initial processing, the net PL remains relatively unchanged for the durations up to 15 minutes. $\lambda_{exc.} = 365$ nm

Figure 5-3 shows the excitonic emission and total integrated emission obtained through constant wave photoluminescence spectroscopy (PL). The reduction of quantum yield (QY) occurring in the first 3 minutes of processing is generally expected as the removal of ZnS is known to de-passivate non-radiative surface recombination sites.[47,49] With the typical thickness of ZnS shell on the order of a monolayer, i.e. $\sim$ 3.1 Å, for core-shell QDs with an optimized quantum yield[47,59] and the average etch rate of $\sim$ 1.3 Å/min in this case, 3 minutes remains sufficient to entirely remove the ZnS shell. This expectedly coincides with the increase of non-radiative recombinations and the reduction of excitonic emission intensity, Figure 5-3(b).

It is critical to note that treatments exceeding up to 5$\times$ the initial period of 3 minutes

*HRTEM diffractogram and lattice constant analysis completed with help by Elaheh Kheirandish.

had no appreciable effect on quantum yield (QY).[†] The surface-to-volume ratio,

$$\eta = \frac{4\pi a^2}{\frac{4}{3}\pi a^3}, \tag{5.1}$$

is to increase as $\sim 1/a$ for smaller diameter QDs and the QY is expected to drop with the etching time since more defects will be present per particle volume. The time-independent QY measured in this case is a likely due to an increase of the oscillator strength of the optical transitions for smaller size 0D systems offsetting the expected QY reduction.

The PL measurements show a consistent blue-shifting of the excitonic peak dependent on processing time. Per HRTEM results, processed QD radii are generally less that of calculated exciton Bohr radius,

$$a_B \approx 53 \times 10^{12} \cdot \frac{\epsilon_r \; m_0}{\mu} = 3.1 \text{ nm} \tag{5.2}$$

suggesting that all samples are adequately confined to exhibit room temperature excitonic emission, (ϵ_r, m_0, and μ are the relative dielectric constant, electron mass at rest, and reduced effective mass, respectively). Furthermore, the assessment that the shell is removed during initial processing implies the measurements of bare-core QDs (processed QDs) can be readily contrasted to the framework of a spherical potential well in the effective mass approximation, as covered in Chapter 2.[29,75]

The ground-state quantum dot exciton energy is,

$$\hbar\omega = E_g - 1.8\frac{e^2}{4\pi\epsilon a} + \frac{\pi^2\hbar^2}{2\mu a^2}, \tag{5.3}$$

where the three summed terms are the bulk material band-gap, Coulomb exciton potential, and quantum confinement of electrons and holes, respectively.

The as-grown QDs have a relative sulfur:selenium ratio of 0.17:0.83 per EDX measure-

[†]Though no explicit quantum yield measurements were completed, the comparisons of QY are made in reference to that of the as-grown $CdSe_{0.83}S_{0.17}$/ZnS QDs.

ments. The linear interpolation ('bowing') formula,

$$E_g(\text{CdSeS}) = (1-x)E_g(\text{CdSe}) - xE_g(\text{CdS}) - bx(1-x) \tag{5.4}$$

can be used to compute the alloy band-gap $E_g(\text{CdSe}_{0.83}\text{S}_{0.17})$, with x standing for sulfur content.[76] In the cited work of Wei et. al, the CdSeS bowing constant, b is reported to be 0.28 eV.[54] Using room temperature bandgaps of 1.74 eV and 2.42 eV for CdSe and CdS, respectively, the alloy bandgap is found to be 1.81 eV.

The value of dielectric content ($\epsilon_r = \epsilon/\epsilon_0 = 6$), effective electron mass ($m_e^* = 0.13\ m_0$) and effective hole mass ($m_h^* = 0.45\ m_0$) for the remaining calculation variables are approximated for the alloy by assuming those of reported bulk CdSe values, due to sulfur content being relatively small to selenium. The measured emission energies and theoretical energy curve, per Eq (5.3),are plotted versus radius in Figure 5-4.

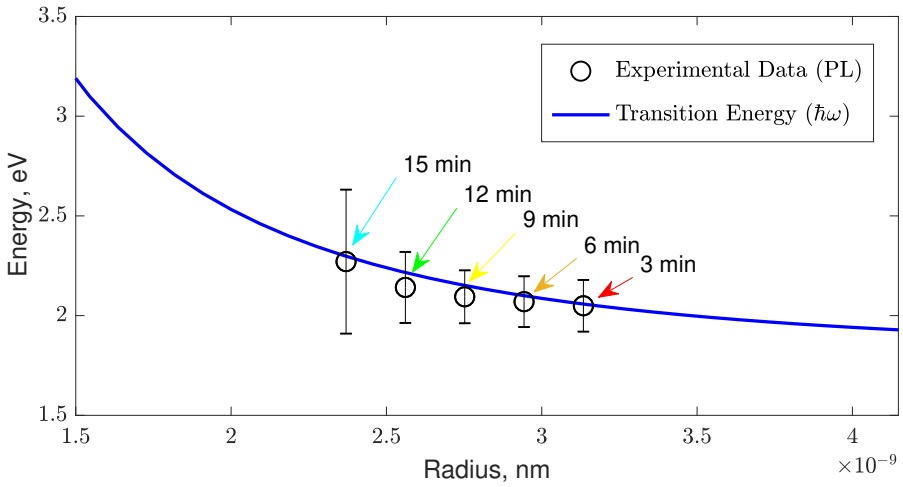

Figure 5-4: Experimental PL excitonic peak energy of processed QDs vs size as determined by HRTEM. The corresponding FWHM is depicted as error bars for each peak. The blue line shows excitonic transition energy ($\hbar\omega$) for $\text{CdSe}_{1-x}\text{S}_x$ QDs per EMA modeling, with sulfur content $x = 0.17$.

The QD diameter size distribution range only changes slightly, per HRTEM results. Thus, the relative diameter range and, in turn, excitonic emission peak broadening are expected to increase with etch time. Furthermore, with the temperature remaining constant, the etch rate remains consistent through processing, resulting in size reduction of QDs at

$\sim$1.3 Å/min. Per Eq (5.3), confinement contribution will outweigh the Coulomb terms as the radius decreases, leading to non-linear spectral shifting with processing time. The non-linear emission broadening and spectral shifting evident in Figure 5-4. The results serve as additional evidence of shifting due to quantum confinement effects. The small deviations can likely be associated with the presence of an unaccounted deviations in alloy content in the QD cores, induced by unbalanced precursor reactivity during synthesis.[49,77,78] However, these inconsistencies seem to be nearly negligible as the experimental and theoretical exciton transition energies are in good agreement. In this context, the outlined QD processing and characterization techniques could provide a useful method of characterizing the homogeneity of alloyed QD structures.

In addition to the excitonic peak, two background peaks were found through Gaussian spectral decomposition. The two PL bands with peaks at $\sim$500 and $\sim$556 nm that constitute background PL, only appear in the processed samples and are therefore assigned to etch reaction byproducts. The intensity and width of the 500 nm peak remains constant for all treatment times, whereas the 556 nm peak is seen to slightly increase in intensity with initial processing time from 3 to 9 minutes, then continues to evolve through 15 minutes. This is shown in Figure 5-5. As etching is clearly taking place, Zn^{2+} and Cd^{2+} being soluble are formed and attributed to defect-associated PL of ZnO and CdO.[79,80]

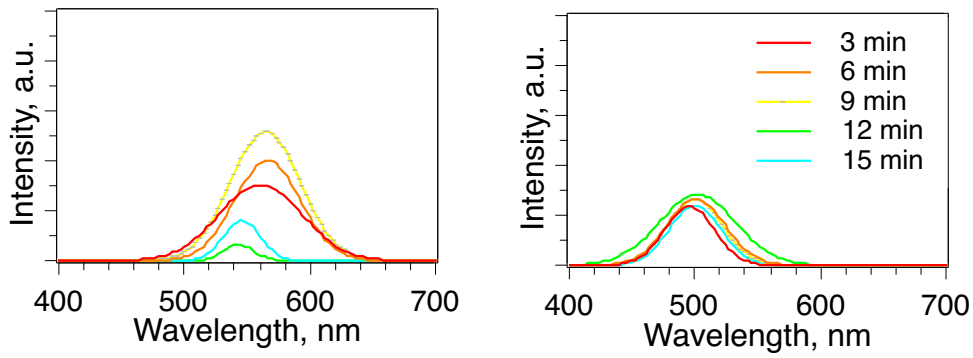

Figure 5-5: Evolution of background cw-PL of etched CdSeS/ZnS QDs with processing durations from 3 to 15 minutes by alcohol. The byproduct emission spectra are consistent with the formation of defect-associated CdO (Left) and ZnO (Right) with respective mean peaks at 500 nm and 556 nm.

5.3 Chemical Pathway

The formation of cadmium and zinc oxides seems to indicate an QD surface oxidation. Oxidation reactions involving water are known to proceed with the involvement of hydroxyl radicals. Since treatments with water alone were ineffective, it is highly unlikely that hydroxyl radicals can form directly on the surface of the as-grown quantum dots, i.e. ZnS-shell. Likewise, the direct oxidation of CdS by water, even in the presence of ambient light, is very unlikely due to a relatively large potential required for hydroxyl radicals to form directly from water.[81] Yet, the QD etch rate remains strongly sensitive to the presence of water.

HRTEM confirms the crystalline bonds within the QD are maintained during processing. Such etching can be interpreted as a physical dissolution process.[69] The above facts suggest that water plays a secondary role by facilitating the dissolution and removal of the reaction intermediates/ byproducts that can otherwise hinder further etching. The weak intermolecular interactions at the QD surface are likely cancelled by the solution and substituted by the interactions with solvate molecules. This is consistent with the stronger intramolecular forces remaining unaffected. In the presence of oxygen, the treatment is likely to involve the surface cascade reactions:

$$(CH_3)_2CHOH + h^+ \xrightarrow{heat} (CH_3)_2COH + H^+ \tag{5.5}$$

$$ZnS + 2H^+ \longrightarrow Zn^{2+} + S + H_2 \tag{5.6}$$

$$CdSeS + 2H^+ \longrightarrow Cd^{2+} + S + Se + H_2 \tag{5.7}$$

$$O_2 + e^- \longrightarrow O_2^- \tag{5.8}$$

$$S + 2O_2^- \longrightarrow SO_4^{2-} \tag{5.9}$$

Both e^- and h^+ are ZnS and CdS surface-supplied charges, likely formed through absorption of stray light. The alcohol supports dissolution at the surface, whereas the water helps dissolve Zn^{2+}, Cd^{2+} and SO_4^{2-}, moving them away from the surface. The metal cations eventually react with oxygen and precipitate in the form of ZnO and CdO.

Chapter 6

Conclusion

6.1 Summary

Colloidal QDs are driving the commercial viability of QD-based technologies. Though colloidal chemistry methods offer low-cost, high quality quantum dot nanocrystal structures, it is an additive, one-way technique that results in QDs of a particular size predetermined during initial synthesis. Additionally, due to Ostwald ripening, synthesis of QDs with sizes below a certain threshold is not feasible with colloidal methods. For the first time, a controllable, complimentary down-sizing technique to colloidally grown QDs is reported.

The size and underlying optoelectronic characteristics of the alloyed QDs in II-VI semiconductors are manipulated using a top-down approach, achieved by performing alcohol-based treatments. According to photoluminescence tests, the emission color evolves from red to green for samples that were treated for up to $\sim$15 mins through a vapor-based sonication method. The spectral evolution is found to be consistent with isotropic size reduction. Spectroscopic studies are corroborated by HRTEM investigations and, in tandem, are in strong agreement with the effective mass approximation model. In contrast to prior-developed top-down semiconductor processing routes, crystallinity, size distribution, and aspect ratio of QDs remain relatively unaffected throughout the processing. The PL results exhibit a steady quantum yield once the shell is removed ($>$ 3 min), confirming a minimal number of defects are created as a side-effect of processing. For the applications requiring

high quantum yields, the restoration of the ZnS cap could be considered as a concluding processing step.

The study presents an technologically viable processing route to achieve post-growth adjustment to the size and, therefore, the optoelectronic characteristics of core-shell, alloyed nano-crystals in II-VI semiconductor systems. With this approach, it should be possible to overcome size limitations due to Ostwald ripening in colloidal synthesis, extending the emission spectrum and application range of alloyed semiconductor QDs.

6.2 Potential Applications

The most impactful attribute of the reported study is the prospect of post-growth QDs with down-tunable diameters through facile alcohol treatment. The processing approach herein could be developed to consistently create previously unobtainable sizes of QDs, unleashing the potential for many new studies of QDs.

In particular, smaller QDs could be exploited in biomedical applications, by enabling even smaller size biologically compatible QD-based probes.[82–84] In addition to ligand exchange, proteins are routinely attached to the shell of the QDs and are used to deploy QDs to a target site within an *in vivo* or *in vitro* specimen.[7,8] The core size has a large effect on the hydrodynamics of the system since the attached protein is comparably small. A smaller QD would allow for additional penetration schemes into tissues and cells, furthering the imaging and drug delivery efforts currently underway. For example, the penetration and accumulation of nanotherapeutics into a tumor cell has been shown to dramatically increase with the use of 10 nm nanoparticles compared to common 100 nm alternatives.[85] A continuation of order-of-magnitude shrinkage could lead to similar drug delivery efficacy improvements. Furthermore, the ultra-small nanoparticle can more readily pass through the renal barrier, minimizing *in vivo* toxicity through renal clearance.

Additionally, it has been shown that the charge injection rate of QD sensitized solar cells (QDSSC) can be directly attributed to QD size.[86] The reported coverage of transport layer in QDSSCs remains low ($< 34\%$) and could benefit from the deposition of smaller

QDs.[87] Therefore, integration of smaller QDs could potentially open pathways to better efficiencies in photovoltaic devices.

The cost of QD manufacturing still stands as a barrier to wide-scale adoption of QD-based devices. The post-growth size-inflexibility inherent to colloidally grown QDs has yet to be overcome. Optimized throughput of single-size colloidal QDs would likely drive down synthesis cost. Through further development of the elementary etching techniques employed in this study, the potential for bulk QD growth followed by inexpensive processing to control final size may be achievable.

Bibliography

[1] A Paul Alivisatos. Perspectives on the Physical Chemistry of Semiconductor Nanocrystals. *The Journal of Physical Chemistry*, 100(31):13226–13239, January 1996.

[2] M A Hines and G D Scholes. Colloidal PbS Nanocrystals with Size-Tunable Near-Infrared Emission: Observation of Post-Synthesis Self-Narrowing of the Particle Size Distribution. *Advanced Materials*, 15(21):1844–1849, November 2003.

[3] Al L Efros and M Rosen. The Electronic Structure of Semiconductor NANOCRYSTALS. *Annual Review of Materials Research*, 30(1):475–521, August 2000.

[4] Kyung-Sang Cho, Eun Kyung Lee, Won-Jae Joo, Eunjoo Jang, Tae-Ho Kim, Sang Jin Lee, Soon-Jae Kwon, Jai Yong Han, Byung-Ki Kim, Byoung Lyong Choi, and Jong Min Kim. High-performance crosslinked colloidal quantum-dot light-emitting diodes. *Nature Photonics*, 3(6):341–345, May 2009.

[5] Future Market Insights. NANOMATERIALS, August 2014.

[6] Xiaohu Gao, Yuanyuan Cui, Richard M Levenson, Leland W K Chung, and Shuming Nie. In vivo cancer targeting and imaging with semiconductor quantum dots. *Nature biotechnology*, 22(8):969–976, August 2004.

[7] Igor L Medintz, H Tetsuo Uyeda, Ellen R Goldman, and Hedi Mattoussi. Quantum dot bioconjugates for imaging, labelling and sensing. *Nature materials*, 4(6):435–446, June 2005.

[8] Ute Resch-Genger, Markus Grabolle, Sara Cavaliere-Jaricot, Roland Nitschke, and Thomas Nann. Quantum dots versus organic dyes as fluorescent labels. *Nature methods*, 5(9):763–775, September 2008.

[9] Xiangyou Liu, Gary B Braun, Mingde Qin, Erkki Ruoslahti, and Kazuki N Sugahara. In vivo cation exchange in quantum dots for tumor-specific imaging. *Nature Communications*, pages 1–12, August 2017.

[10] Yasuhiro Shirasaki, Geoffrey J Supran, Moungi G Bawendi, and Vladimir Bulović. Emergence of colloidal quantum-dot light-emitting technologies. *Nature Photonics*, 7(1):13–23, January 2013.

[11] Elise Talgorn, Yunan Gao, Michiel Aerts, Lucas T Kunneman, Juleon M Schins, T J Savenije, Marijn A van Huis, Herre S J van der Zant, Arjan J Houtepen, and Laurens D A Siebbeles. Unity quantum yield of photogenerated charges and band-like transport in quantum-dot solids. *Nature Nanotechnology*, 6(1):733–739, November 2011.

[12] Ou Chen, Jing Zhao, Vikash P Chauhan, Jian Cui, Cliff Wong, Daniel K Harris, He Wei, Hee-Sun Han, Dai Fukumura, Rakesh K Jain, and Moungi G Bawendi. Compact high-quality CdSe–CdS core–shell nanocrystals with narrow emission linewidths and suppressed blinking. *Nature materials*, 12(5):445–451, February 2013.

[13] J M Caruge, J E Halpert, V Wood, V Bulović, and M G Bawendi. Colloidal quantum-dot light-emitting diodes with metal-oxide charge transport layers. *Nature Photonics*, 2(4):247–250, March 2008.

[14] Hilmi Volkan Demir, Sedat Nizamoglu, Talha Erdem, Evren Mutlugun, Nikolai Gaponik, and Alexander Eychmüller. Quantum dot integrated LEDs using photonic and excitonic color conversion. *Nano Today*, 6(6):632–647, December 2011.

[15] Steven A McDonald, Gerasimos Konstantatos, Shiguo Zhang, Paul W Cyr, Ethan J D Klem, Larissa Levina, and Edward H Sargent. Solution-processed PbS quantum dot infrared photodetectors and photovoltaics. *Nature materials*, 4(2):138–142, January 2005.

[16] Qing Shen, Junya Kobayashi, Lina J Diguna, and Taro Toyoda. Effect of ZnS coating on the photovoltaic properties of CdSe quantum dot-sensitized solar cells. *Journal of Applied Physics*, 103(8):084304, April 2008.

[17] Prashant V Kamat. Quantum Dot Solar Cells. Semiconductor Nanocrystals as Light Harvesters. *The Journal of Physical Chemistry C*, 112(48):18737–18753, November 2008.

[18] Wanli Ma, Joseph M Luther, Haimei Zheng, Yue Wu, and A Paul Alivisatos. Photovoltaic Devices Employing Ternary PbSxSe1-x Nanocrystals. *Nano Letters*, 9(4):1699–1703, March 2009.

[19] Prashant V Kamat. Quantum Dot Solar Cells. The Next Big Thingin Photovoltaics. *The Journal of Physical Chemistry Letters*, 4(6):908–918, March 2013.

[20] K W Song, R Costi, and V Bulović. Electrophoretic Deposition of CdSe/ZnS Quantum Dots for Light-Emitting Devices. *Wiley Online Library*, 2013.

[21] F Pelayo García de Arquer, Ardalan Armin, Paul Meredith, and Edward H Sargent. Solution-processed semiconductors for next-generation photodetectors. *Nature Reviews Materials*, 2(3):13424–16, January 2017.

[22] P Michler, A Kiraz, C Becher, W V Schoenfeld, P M Petroff, Lidong Zhang, E Hu, and A Imamoglu. A Quantum Dot Single-Photon Turnstile Device. *Science (New York, N.Y.)*, 290(5500):2282–2285, December 2000.

[23] Rudolf Bratschitsch and Alfred Leitenstorfer. Artificial atoms for quantum optics. *Nature materials*, 5(11):855–856, November 2006.

[24] Robert H Hadfield. Single-photon detectors for optical quantum information applications. *Nature Photonics*, 3(12):696–705, December 2009.

[25] M D Eisaman, J Fan, A Migdall, and S V Polyakov. Invited Review Article: Single-photon sources and detectors. *Review of Scientific Instruments*, 82(7):071101–26, July 2011.

[26] U.S. E.I.A. Frequently Asked Questions How much electricity is used for lighting in the United States? pages 1–2, December 2018.

[27] US Department of Energy. LED Efficacy: What America Stands to Gain, October 2017.

[28] J R Brodrick. DOE Solid-State Lighting Program, 2015.

[29] A I Ekimov and A A Onushchenko. Quantum size effect in three-dimensional microscopic semiconductor crystals. *Journal of Experimental and Theoretical Physics Letters*, 34:345–, September 1981.

[30] Ch Heyn, A Stemmann, A Schramm, H Welsch, W Hansen, and Á Nemcsics. Regimes of GaAs quantum dot self-assembly by droplet epitaxy. *Physical Review B*, 76(7):075317, August 2007.

[31] V B Verma, M J Stevens, K L Silverman, NL Dias Optics, and 2011. Photon antibunching from a single lithographically defined InGaAs/GaAs quantum dot. *osapublishing.org*.

[32] Andrew Griffiths. Exploring MBE Growth Of Quantum Dots: Low Density Growth For Quantum Information Devices. 2014.

[33] Vitaly Shchukin, Eckehard Schöll, and Peter Kratzer. Thermodynamics and Kinetics of Quantum Dot Growth. Springer Berlin Heidelberg, Berlin, Heidelberg, 2008.

[34] Y Arakawa and H Sakaki. Multidimensional quantum well laser and temperature dependence of its threshold current. *Applied Physics Letters*, 40(11):939–941, August 1998.

[35] D Leonard, K Pond, and P M Petroff. Critical layer thickness for self-assembled InAs islands on GaAs. *Physical Review B*, 50(16):11687–11692, October 1994.

[36] Xiaogang Peng, Michael C Schlamp, Andreas V Kadavanich, and A Paul Alivisatos. Epitaxial Growth of Highly Luminescent CdSe/CdS Core/Shell Nanocrystals with Photostability and Electronic Accessibility. *Journal of the American Chemical Society*, 119(30):7019–7029, July 1997.

[37] Arto Nurmikko. What future for quantum dot-based light emitters? *Nature Publishing Group*, 10(12):1001–1004, December 2015.

[38] H T Johnson and L B Freund. Mechanics of coherent and dislocated island morphologies in strained epitaxial material systems. *Journal of Applied Physics*, 81(9):6081–6090, June 1998.

[39] L E Brus. A simple model for the ionization potential, electron affinity, and aqueous redox potentials of small semiconductor crystallites. *The Journal of Chemical Physics*, 79(1):5566–5571, December 1983.

[40] L E Brus. Electron-electron and electron-hole interactions in small semiconductor crystallites: The size dependence of the lowest excited electronic state. *The Journal of Chemical Physics*, 80(9):4403–4409, May 1984.

[41] M G Bawendi, A R Kortan, M L Steigerwald, and L E Brus. X-ray structural characterization of larger CdSe semiconductor clusters. *The Journal of Chemical Physics*, 91(1):7282–7290, December 1989.

[42] A Paul Alivisatos, A L Harris, N J Levinos, M L Steigerwald, and L E Brus. Electronic states of semiconductor clusters: Homogeneous and inhomogeneous broadening of the optical spectrum. *The Journal of Chemical Physics*, 89(7):4001–4011, October 1988.

[43] C B Murray, D J Norris, and M G Bawendi. Synthesis and characterization of nearly monodisperse CdE (E = sulfur, selenium, tellurium) semiconductor nanocrystallites. *Journal of the American Chemical Society*, 115(19):8706–8715, 1993.

[44] C B Murray. *Synthesis and characterization of II-VI quantum dots and their assembly into 3D quantum dot superlattices. ...* CHEMICAL SOC 1155 16TH ST, September 1995.

[45] Michael A Boles, Daishun Ling, Taeghwan Hyeon, and Dmitri V Talapin. The surface science of nanocrystals. *Nature materials*, 15(3):364–, March 2016.

[46] Irina Lokteva, Nikolay Radychev, Florian Witt, Holger Borchert, Jürgen Parisi, and Joanna Kolny-Olesiak. Surface Treatment of CdSe Nanoparticles for Application in Hybrid Solar Cells: The Effect of Multiple Ligand Exchange with Pyridine. *The Journal of Physical Chemistry C*, 114(29):12784–12791, June 2010.

[47] B O Dabbousi, J Rodriguez-Viejo, F V Mikulec, J R Heine, H Mattoussi, R Ober, K F Jensen, and M G Bawendi. (CdSe)ZnS Core Shell Quantum Dots: Synthesis and Characterization of a Size Series of Highly Luminescent Nanocrystallites. *The Journal of Physical Chemistry B*, 101(46):9463–9475, November 1997.

[48] Margaret A Hines and Philippe Guyot-Sionnest. Synthesis and Characterization of Strongly Luminescing ZnS-Capped CdSe Nanocrystals. *The Journal of Physical Chemistry*, 100(2):468–471, January 1996.

[49] Robert E Bailey and Shuming Nie. Alloyed semiconductor quantum dots: tuning the optical properties without changing the particle size. *Journal of the American Chemical Society*, 125(23):7100–7106, June 2003.

[50] Zhengtao Deng, Hao Yan, and Yan Liu. Band Gap Engineering of Quaternary-Alloyed ZnCdSSe Quantum Dots via a Facile Phosphine-Free Colloidal Method. *Journal of the American Chemical Society*, 131(49):17744–17745, November 2009.

[51] Tangi Aubert, Marco Cirillo, Stijn Flamee, Rik Van Deun, Holger Lange, Christian Thomsen, and Zeger Hens. Homogeneously Alloyed CdSe 1– xS xQuantum Dots ($0 \leq x \leq 1$): An Efficient Synthesis for Full Optical Tunability. *Chemistry of Materials*, 25(12):2388–2390, June 2013.

[52] Nguyen T K Thanh, N Maclean, and S Mahiddine. Mechanisms of Nucleation and Growth of Nanoparticles in Solution. *ACS Publications*, July 2014.

[53] Peter Y Yu and Manuel Cardona. Fundamentals of Semiconductors: Physics and Materials Properties, 4th Edition. pages 1–793, April 2010.

[54] Su-Huai Wei, S B Zhang, and Alex Zunger. First-principles calculation of band offsets, optical bowings, and defects in CdS, CdSe, CdTe, and their alloys. *Journal of Applied Physics*, 87(3):1304–1311, February 2000.

[55] Susumu Ninomiya and Sadao Adachi. Optical properties of cubic and hexagonal CdSe. *Journal of Applied Physics*, 78(7):4681–4689, October 1995.

[56] Y S Park and D C Reynolds. Exciton Structure in Photoconductivity of CdS, CdSe, and CdS: Se Single Crystals. *Physical Review*, 132(6):2450–2457, 1963.

[57] Ivan Pelant and Jan Valenta. Luminescence of excitons. Oxford University Press, 2012.

[58] A Paul Alivisatos. Semiconductor Clusters, Nanocrystals, and Quantum Dots. *Science (New York, N.Y.)*, 271(5):933–937, February 1996.

[59] Jonathan S Steckel, John P Zimmer, Seth Coe Sullivan, Nathan E Stott, Vladimir Bulović, and Moungi G Bawendi. Blue Luminescence from (CdS)ZnS Core Shell Nanocrystals. *Angewandte Chemie International Edition*, 43(16):2154–2158, April 2004.

[60] Jennifer A Hollingsworth. *Semiconductor Nanocrystal Quantum Dots*, volume 23. John Wiley & Sons, Ltd, Chichester, UK, December 2011.

[61] M A Baldo, D F O'Brien, Y You, A Shoustikov, S Sibley, M E Thompson, and S R Forrest. Highly efficient phosphorescent emission from organic electroluminescent devices. *Nature*, 395(6698):151–154, September 1998.

[62] Wei Wang, Wenliang Feng, Jun Du, Weinan Xue, Linlin Zhang, Leilei Zhao, Yan Li, and Xinhua Zhong. Cosensitized Quantum Dot Solar Cells with Conversion Efficiency over 12%. *Advanced Materials*, 30(11):1705746, March 2018.

[63] O E Semonin, J M Luther, S Choi, H Y Chen, J Gao, A J Nozik, and M C Beard. Peak External Photocurrent Quantum Efficiency Exceeding 100in a Quantum Dot Solar Cell. *Science (New York, N.Y.)*, 334(6062):1530–1533, December 2011.

[64] T Edvinsson. Optical quantum confinement and photocatalytic properties in two-, one- and zero-dimensional nanostructures. *Royal Society Open Science*, 5(9):180387–17, September 2018.

[65] K F Riley, M P Hobson, and S J Bence. *Mathematical Methods for Physics and Engineering*. A Comprehensive Guide. Cambridge University Press, March 2006.

[66] David J Griffiths. Introduction to Quantum Mechanics. *Introduction to quantum mechanics/ David J. Griffiths. Englewood Cliffs*, 1995.

[67] Tadd Kippeny, Laura A Swafford, and Sandra J Rosenthal. Semiconductor Nanocrystals: A Powerful Visual Aid for Introducing the Particle in a Box. *Journal of Chemical Education*, 79(9):1094–, September 2002.

[68] M G Bawendi, M L Steigerwald, and L E Brus. The Quantum Mechanics of Larger Semiconductor Clusters ("Quantum Dots"). *Annual Review of Physical Chemistry*, 41(1):477–496, October 1990.

[69] Michael Kohler. *Etching in Microsystem Technology*. Weinheim ; New York : Wiley-VCH, 1999.

[70] A Henglein. Catalysis of photochemical reactions by colloidal semiconductors. *Pure and Applied Chemistry*, 56(9):1215–1224, 1984.

[71] Y Yang Leng. *Materials characterization : introduction to microscopic and spectroscopic methods*. Singapore ; Hoboken, NJ : J. Wiley, 2008.

[72] Takeshi Aoki. Photoluminescence Spectroscopy. John Wiley & Sons, Inc., Hoboken, NJ, USA, 2012.

[73] Horiba. Fluorolog 3 Operation Manual. pages 1–250, October 2002.

[74] Th Hahn. *International Tables for Crystallography* . June 2008.

[75] Al L Efros and M Rosen. Quantum size level structure of narrow-gap semiconductor nanocrystals: Effect of band coupling. *Physical Review B (Condensed Matter and Materials Physics)*, 58(1):7120–7135, September 1998.

[76] James E Bernard and Alex Zunger. Electronic structure of ZnS, ZnSe, ZnTe, and their pseudobinary alloys. *Physical Review B (Condensed Matter)*, 36(6):3199–3228, August 1987.

[77] Jianying Ouyang, Christopher I Ratcliffe, David Kingston, Baptiste Wilkinson, Jasmijn Kuijper, Xiaohua Wu, John A Ripmeester, and Kui Yu. Gradiently Alloyed Zn xCd 1-xS Colloidal Photoluminescent Quantum Dots Synthesized via a Noninjection One-Pot Approach. *The Journal of Physical Chemistry C*, 112(13):4908–4919, March 2008.

[78] Danielle K Smith, Joseph M Luther, Octavi E Semonin, Arthur J Nozik, and Matthew C Beard. Tuning the Synthesis of Ternary Lead Chalcogenide Quantum Dots by Balancing Precursor Reactivity. *ACS Nano*, 5(1):183–190, December 2010.

[79] Yow-Jon Lin, Chia-Lung Tsai, Yang-Ming Lu, and Chia-Jyi Liu. Optical and electrical properties of undoped ZnO films. *Journal of Applied Physics*, 99(9):093501–5, May 2006.

[80] S K Vasheghani Farahani, V Muñoz-Sanjosé, J Zúñiga-Pérez, C F McConville, and T D Veal. Temperature dependence of the direct bandgap and transport properties of CdO. *Applied Physics Letters*, 102(2):022102–5, January 2013.

[81] George V Buxton, Clive L Greenstock, W Phillips Helman, and Alberta B Ross. Critical Review of rate constants for reactions of hydrated electrons, hydrogen atoms and hydroxyl radicals (OH/O^-)in Aqueous Solution. *Journal of Physical and Chemical Reference Data*, 17(2):513–886, April 1988.

[82] Pavel Zrazhevskiy, Mark Sena, and Xiaohu Gao. Designing multifunctional quantum dots for bioimaging, detection, and drug delivery. *Chem. Soc. Rev.*, 39(11):4326–29, 2010.

[83] Ajmeeta Sangtani, Eleonora Petryayeva, Miao Wu, Kimihiro Susumu, Eunkeu Oh, Alan L Huston, Guillermo Lasarte-Aragones, Igor L Medintz, W Russ Algar, and James B Delehanty. Intracellularly Actuated Quantum Dot–Peptide–Doxorubicin Nanobioconjugates for Controlled Drug Delivery via the Endocytic Pathway. *Bioconjugate Chemistry*, 29(1):136–148, December 2017.

[84] Janet Y Sheung, Pinghua Ge, Sung Jun Lim, Sang Hak Lee, Andrew M Smith, and Paul R Selvin. Structural Contributions to Hydrodynamic Diameter for Quantum Dots Optimized for Live-Cell Single-Molecule Tracking. *The Journal of Physical Chemistry C*, 122(30):17406–17412, July 2018.

[85] Cliff Wong, Triantafyllos Stylianopoulos, Jian Cui, John Martin, Vikash P Chauhan, Wen Jiang, Zoran Popović, Rakesh K Jain, Moungi G Bawendi, and Dai Fukumura. Multistage nanoparticle delivery system for deep penetration into tumor tissue. In *Proceedings of the National Academy of Sciences*, pages 2426–2431. Department of Chemistry, Massachusetts Institute of Technology, Cambridge, MA 02139, February 2011.

[86] Hyeong Jin Yun, Taejong Paik, Benjamin Diroll, Michael E Edley, Jason B Baxter, and Christopher B Murray. Nanocrystal Size-Dependent Efficiency of Quantum Dot Sensitized Solar Cells in the Strongly Coupled CdSe Nanocrystals/TiO 2System. *ACS Applied Materials & Interfaces*, 8(23):14692–14700, June 2016.

[87] Zhenxiao Pan, Huashang Rao, Iván Mora-Seró, Juan Bisquert, and Xinhua Zhong. Quantum dot-sensitized solar cells. *Chem. Soc. Rev.*, 47(20):7659–7702, 2018.